

## CAMS newly detected meteor showers and the sporadic background



P. Jenniskens<sup>a,b,\*</sup>, Q. Nénon<sup>a</sup>, P.S. Gural<sup>c</sup>, J. Albers<sup>a</sup>, B. Haberman<sup>a</sup>, B. Johnson<sup>a</sup>, R. Morales<sup>d</sup>, B.J. Grigsby<sup>a,e</sup>, D. Samuels<sup>d</sup>, C. Johannink<sup>f</sup>

<sup>a</sup>SETI Institute, Carl Sagan Center, 189 Bernardo Avenue, Mountain View, CA 94043, USA

<sup>b</sup>NASA Ames Research Center, Mail Stop 241-11, Moffett Field, CA 95035, USA

<sup>c</sup>Leidos, 14668 Lee Road, Chantilly, VA 20151, USA

<sup>d</sup>Fremont Peak Observatory Association, P.O. Box 1376, San Juan Bautista, CA 95045, USA

<sup>e</sup>Lick Observatory, U.C. Santa Cruz, 7281 Mount Hamilton Road, CA 95140, USA

<sup>f</sup>Dutch Meteor Society, Schiefstrasse 36, D 48599 Gronau, Germany

### ARTICLE INFO

#### Article history:

Received 16 June 2015

Revised 15 September 2015

Accepted 1 November 2015

Available online 17 November 2015

#### Keywords:

Meteors

Comets, dust

Interplanetary dust

Near-Earth objects

Asteroids

### ABSTRACT

The *Cameras for Allsky Meteor Surveillance* (CAMS) video-based meteoroid orbit survey adds 60 newly identified showers to the IAU Working List of Meteor Showers (numbers 427, 445–446, 506–507, and part of 643–750). 28 of these are also detected in the independent SonotaCo survey. In total, 230 meteor showers and shower components are identified in CAMS data, 177 of which are detected in at least two independent surveys. From the power-law size frequency distribution of detected showers, we extrapolate that 36% of all CAMS-observed meteors originated from  $\sim 700$  showers above the  $N = 1$  per 110,000 shower limit. 71% of mass falling to Earth from streams arrives on Jupiter-family type orbits. The transient Geminids account for another 15%. All meteoroids not assigned to streams form a sporadic background with highest detected numbers from the apex source, but with 98% of mass falling in from the antihelion source. Even at large  $\sim 7$ -mm sizes, a Poynting–Robertson drag evolved population is detected, which implies that the Grün et al. collisional lifetimes at these sizes are underestimated by about a factor of 10. While these large grains survive collisions, many fade on a  $10^4$ -y timescale, possibly because they disintegrate into smaller particles by processes other than collisions, leaving a more resilient population to evolve.

The meteors assigned to the various showers are identified in the CAMS Meteoroid Orbit Database 2.0 submitted to the IAU Meteor Data Center, and can be accessed also at <http://cams.seti.org>.

© 2015 Published by Elsevier Inc.

### 1. Introduction

Meteor showers manifest when comets and active asteroids shed dust and the resulting meteoroid streams evolve to intersect Earth's orbit. These showers infer the parent comet orbit, the epoch of past activity, and the manner in which this material now is dispersed in the inner Solar System. The showers trace the source of all zodiacal dust and play a role in satellite impact hazard and planetary defense studies (Jenniskens, 2006; Williams, 2011).

Since October of 2010, we have conducted a meteor shower survey to map as many as possible of our nighttime meteor showers using low-light-level video imaging and triangulation of  $-1$  to  $+4$  magnitude meteors. This *Cameras for Allsky Meteor Surveillance* (CAMS) project was conceived to validate the unconfirmed

showers in the International Astronomical Union's (IAU) Working List of Meteor Showers (Jenniskens et al., 2011). The list maintains a unique system of nomenclature intended to keep the literature transparent. New showers are added regularly from showers detected in ongoing meteoroid orbit surveys (Jenniskens et al., 2009; Brown et al., 2010; Veres and Tóth, 2010; Segon et al., 2014; Andreic et al., 2014; Koukal et al., 2014; Jopek and Kanuchová, 2014).

At the end of March 2013, when the CAMS meteoroid orbit database had reached 110,000 orbits, we conducted a search for showers in maps of sun-centered ecliptic coordinates of the radiant, by searching for preferred directions in which meteoroids would approach us (the radiant). As many as 70 of the 95 established showers in the IAU Working List were detected (Jenniskens et al., in 2016a). Other established showers are either periodic in nature, or daytime showers, southern hemisphere showers, or showers rich in faint meteors that are not easily observed. Only the Southern  $\iota$ -Aquiriids were not detected, while

\* Corresponding author at: SETI Institute, Carl Sagan Center, 189 Bernardo Avenue, Mountain View, CA 94043, USA. Fax: +1 650 962 9419.

E-mail address: [Petrus.M.Jenniskens@nasa.gov](mailto:Petrus.M.Jenniskens@nasa.gov) (P. Jenniskens).

they should have been. Jenniskens et al. (2016a) also identified 26 new shower components. Subsequently, Jenniskens et al. (2016b) discussed the showers already in the Working List that needed verification, 41 of which were confirmed.

CAMS also detected many new showers. In dedicated papers, we focused on some strong detections, including the February  $\eta$ -Draconids (#427, FED) (Jenniskens and Gural, 2011), the  $\kappa$ -Ursae Majorids (#445, KUM) and the December  $\phi$ -Cassiopeiids (#446, DPC) (Jenniskens, 2012; Jenniskens et al., 2012), the February  $\varepsilon$ -Virginids (#506, FEV) (Steakley and Jenniskens, 2013), and the  $\upsilon$ -Andromedids (#507, UAN) (Holman and Jenniskens, 2013).

That still left a large number of unassigned potential meteor showers. In a previous paper, we reported on showers #448–502 derived from an automated high threshold single-linked D-criterion search, which resulted in 54 possible detections (Rudawska and Jenniskens, 2014). After removing four duplicates with showers already in the IAU Working List, nineteen showers were confirmed by showing that these were also detected in the independent SonotaCo video meteor database (Jenniskens and Nénon, 2016). Three other showers were convincingly detected only in one survey, but not in the other, and need further observations to be confirmed. The SonotaCo survey uses similar low-light-level video techniques for meteor triangulation (Kanamori et al., 2009). For a comparison of both projects, see Jenniskens et al. (2011).

In this paper, we discuss showers #643–750 of the IAU Working List, which are newly identified showers extracted from CAMS observations up to the end of March 2013. By the end of March 2015, the CAMS database had more than doubled in size. This new data will be used now to verify the earlier detections (Section 3), but not to identify further showers or improve the median orbital elements of each shower, a task postponed to a future paper. Now all obvious showers in CAMS data have been identified, the statistical properties of the shower population are discussed in Section 4. After removing all identified showers from the database, the statistical properties of the remaining sporadic meteors are discussed in Section 5.

## 2. Methods

The CAMS hardware and software are described in Jenniskens et al. (2011) and Gural (2012). Over 60 low-light video cameras are deployed at three stations in California (+37°N) and a growing number of cameras operate in a distributed network in the BeNeLux (+52°N) (Bettonvil et al., 2014). Meteors of  $-1$  to  $+4$  visual magnitude are typically recorded. Directions are calibrated against average frames integrated for 8-s, which show stars to limiting magnitude of  $+8.1$ . The astrometric data are then triangulated to derive trajectories (entry speed and radiant of the entry vector), as well as pre-atmospheric orbits.

At the end of March 2013, the California network had collected 109,548 meteoroid orbits with a precision better than  $2^\circ$  in Right Ascension (median  $0.40^\circ$ ) and better than 10% in entry speed (median 0.89%). The BeNeLux network added another 973 meteoroid orbits.

Meteor showers were identified using an interactive data analysis application called *CAMS StreamFinder*. The program computes the sun-centered ecliptic coordinates of the radiant after drift-correcting for Earth's motion around the Sun (ecliptic longitude of the radiant drifting by  $1^\circ/\text{day}$  and the ecliptic latitude drifting by  $0^\circ/\text{day}$ ). These drift-corrected radiant maps, together with the corresponding maps that plot inclination as a function of longitude of perihelion (the  $II-i$  diagram), were visually inspected in intervals of  $10^\circ$  in solar longitude (and again off-set by  $5^\circ$ ) for areas of higher surface density.

Detected clumps were extracted using the  $D_h$  discriminant criterion (Jopek, 1993), taking care to isolate a group from the local background within the confines of the visually recognizable surface density enhancement so that a smooth background remains.

Once all previously reported meteor showers were identified (Jenniskens et al., 2016a, 2016b; Jenniskens and Nénon, 2016), a large number of clumps in CAMS data remained unassigned. These clumps were extracted in the same manner. In preparation of publication, these showers were added to the Working List as numbers 643–750.

The question remained how significant were these extracted clusters in relation to random variations in surface density of a background population, which consists of diffuse source regions in radiant and orbital element space. A stream-to-background ( $S/B$ ) surface density ratio was calculated, which is the number of assigned stream members inside the  $2\sigma$  contour of the distribution over that in the nearby background (both unassigned and previously assigned meteors), averaged over a four times bigger area.  $S/B = 1$  means that the shower raised the local surface density of radiants a factor of two above the sporadic background. Typically,  $S/B \leq 2$  would constitute a tentative detection, while values larger than 3 are strong detections.

In addition, we can now compare the results to more recent CAMS data and the 168,026 measured orbits so far published by the SonotaCo network in Japan (Kanamori, 2009). At the end of March, 2015, the CAMS database had grown to 257,218 orbits, 18,395 of which were measured by the BeNeLux network. This more than doubled the database and made it possible to use the extended database to validate the earlier detections.

## 3. Results

The newly detected showers are shown in the drift-corrected radiant maps of Figs. 1–12. In each diagram, the left panel shows the CAMS data (Oct. 2010–March 2015) and the right panel the published SonotaCo data (2007–2013).

Radiant coordinates and median orbital elements for each shower are listed in Tables 1–3. Each table lists the number of meteors extracted in the March 2013 database, the median solar longitude of the sample, the median radiant position of drift-corrected radiant coordinates to that solar longitude value, the entry speed, orbital elements, and the Tisserand parameter with respect to Jupiter ( $T_J$ ). Table 4 gives additional information on the duration of activity, the dispersion of the radiant in drift-corrected coordinates, the dispersion of speed, the radiant drift rate, and the stream to background surface density ratio.

### 3.1. Previously discussed showers

The new shower detections will now be discussed in order of their inclusion in the IAU Working List, starting with the five new showers that were previously discussed. We show here how they are detected in the most recent CAMS data and in the SonotaCo database.

Over a period of a few hours on February 4, 2011, a compact cluster of 6 meteors was observed in orbits identical to within measurement error, arriving from a high latitude region of the sky where the sporadic background activity was low (Fig. 1A). This shower is now called the February  $\eta$ -Draconids (#427, FED). This is likely a transient shower, possibly from crossing the 1-revolution dust trail of a long-period comet (Jenniskens and Gural, 2011). Since that time, no shower meteors were detected in 2012, but three in 2013, five in 2014, and two in 2015. The shower was also detected by SonotaCo, with one candidate FED in 2007, one in 2011, and two in 2012 (right panel of Fig. 1A).

**Table 1**  
Newly identified showers with median  $T_J \geq 2.0$  and candidate parent bodies.

IAU <sup>a</sup>	Object	<i>N</i>	$\lambda_o$	R.A.	Dec.	$V_g$	<i>a</i>	<i>q</i>	<i>e</i>	<i>i</i>	$\omega$	Node	$\Pi$	$T_J$
446 <sup>b</sup>	DPC	68	252	19.5	+57.7	16.5	3.10	0.896	0.714	18.0	218.7	252.1	110.9	2.71
	?3D/Biela	<i>H</i>	230.8	23.9	+25.9	17.2	3.49	0.798	0.772	7.1	236.3	230.8	107.1	2.52
644 <sup>b</sup>	JLL	24	288	140.2	+23.4	38.6	1.84	0.098	0.947	22.4	327.3	277.7	246.8	3.12
651 <sup>b</sup>	OAV	8	16	202.0	−13.5	28.9	2.36	0.392	0.842	4.7	109.8	197.4	308.1	2.93
656	AAA	6	31	159.1	−33.8	14.1	2.60	0.941	0.639	13.8	32.6	211.5	244.3	3.06
658 <sup>b</sup>	MBE	18	41	313.6	+71.8	23.5	2.80	0.961	0.657	37.2	151.9	41.3	192.6	2.74
660	EPS	6	49	251.5	−31.0	39.2	2.64	0.127	0.952	24.3	143.4	229.6	13.4	2.37
664	MXA	14	46	88.4	+58.7	11.7	2.41	0.958	0.603	10.4	150.1	47.4	199.6	3.23
680	JEA	8	85	46.7	+27.1	39.1	1.45	0.059	0.960	37.6	23.4	84.6	108.4	3.82
	*C/2002 V5	<i>H</i>	81.1	48.9	+24.8	46.3	<i>Inf.</i>	0.051	1.000	34.1	25.8	81.1	106.9	–
684	JOE	5	89	267.4	−11.2	21.3	2.18	0.617	0.718	8.3	266.1	88.5	355.5	3.28
	?2007 AB12	<i>H</i>	86.2	262.1	−12.2	20.6	2.31	0.651	0.718	7.3	262.0	86.2	348.2	3.17
689	TAC	15	121	311.7	−15.7	28.2	2.59	0.393	0.849	2.4	289.5	120.9	50.1	2.75
	?2005 ET70	<i>H</i>	115.2	307.8	−14.8	28.0	2.13	0.365	0.829	5.6	294.5	115.2	49.7	3.15
692 <sup>b</sup>	EQA	23	138	310.5	−5.8	19.9	2.50	0.685	0.729	7.4	256.9	138.7	35.5	3.02
703 <sup>b</sup>	IOD	12	157	232.3	+53.3	17.8	2.93	0.990	0.664	26.1	161.5	157.2	318.8	2.78
706 <sup>b</sup>	ZPI	14	172	19.8	+9.7	38.2	1.74	0.064	0.960	5.2	335.5	172.4	147.5	3.31
710 <sup>b</sup>	IOL	19	317	172.2	+10.1	40.4	1.59	0.054	0.967	25.8	337.6	317.0	293.7	3.54
712	FDC	5	339	288.8	+46.8	32.0	3.77	0.905	0.760	51.5	143.5	338.8	121.3	2.07
724	LAP	6	268	353.4	−1.8	8.1	2.69	0.984	0.633	0.2	178.1	268.3	86.2	3.06
	?2010 UM7	<i>H</i>	301.6	335.8	−8.5	12.5	2.79	0.891	0.681	0.5	140.1	301.6	81.7	2.93
726 <sup>b</sup>	DEG	17	268	96.7	+25.6	26.8	2.26	0.420	0.816	2.3	285.6	268.0	194.2	3.07
732	FGV	14	338	191.6	−3.0	41.2	1.50	0.036	0.980	8.7	342.4	337.4	320.5	3.40
733	LAL	8	340	144.8	+23.8	15.6	2.64	0.829	0.683	4.0	233.1	340.2	213.9	3.01
	?2011 YH28	<i>H</i>	328.3	141.8	+27.8	18.0	2.62	0.756	0.712	6.3	244.3	328.3	212.6	2.97
746 <sup>b</sup>	EVE	9	252	129.5	−44.2	44.4	2.67	0.976	0.637	78.8	13.2	71.8	86.8	2.16
749 <sup>b</sup>	NMV	13	339	189.1	+3.0	42.7	2.40	0.071	0.979	23.7	332.5	338.9	310.3	2.42
750 <sup>b</sup>	SMV	12	344	188.1	−8.8	40.8	2.02	0.095	0.966	18.5	149.5	164.2	311.1	2.61

<sup>a</sup> In this and following tables, the header symbols have the following meaning: IAU number; object = IAU meteor shower code or parent body designation (with parent bodies labeled “\*” = probable or “?” = possible); *N* = number of observed meteors;  $\lambda_o$  = median solar longitude of the distribution; position of the radiant: R.A. = Right Ascension and Dec. = declination (°, J2000);  $V_g$  = geocentric entry speed in km/s (without Earth's gravitational acceleration); orbital elements in equinox J2000: *a* = semi-major axis (AU), *q* = perihelion distance (AU), *i* = inclination (°),  $\omega$  = argument of perihelion (°), Node = ascending node (°),  $\Pi$  = longitude of perihelion (°);  $T_J$  = Tisserand parameter with respect to Jupiter. The candidate parent body orbit is adjusted to intersect Earth's orbit by variation of the argument of perihelion and inclination (method “H” of Neslusan et al. (1998)).

<sup>b</sup> Shower confirmed in this work by also being detected in SonotaCo data.

**Table 2**  
Newly identified showers with median  $T_J < 2.0$  in retrograde orbits.

IAU	Object	<i>N</i>	$\lambda_o$	R.A.	Dec.	$V_g$	<i>a</i>	<i>q</i>	<i>e</i>	<i>i</i>	$\omega$	Node	$\Pi$	$T_J$
445 <sup>a</sup>	KUM	8	225	147.2	+45.0	65.7	<i>Inf.</i>	0.988	1.000	129.6	185.9	224.0	50.7	−0.01
506 <sup>a</sup>	FEV	55	314	200.4	+11.0	62.9	8.28	0.491	0.954	138.0	272.5	312.6	224.6	−0.14
507 <sup>a</sup>	UAN	28	96	7.1	+40.3	59.3	8.85	0.849	0.910	117.8	130.0	101.0	232.4	0.02
645	PHC	10	190	121.1	+29.3	67.8	4.63	0.761	0.880	163.3	120.3	195.0	313.2	−0.17
652 <sup>a</sup>	OSP	9	18	274.1	−12.3	68.3	2.87	0.824	0.903	160.3	233.8	17.8	249.5	−0.40
655	APC	10	32	313.5	−26.6	69.6	8.00	0.969	0.911	164.7	337.8	212.6	191.9	−0.67
657	GSG	6	30	269.6	−29.0	62.1	3.82	0.373	0.906	166.2	109.3	210.6	319.8	0.69
667 <sup>a</sup>	JTP	19	70	355.8	+7.9	66.6	6.93	0.719	0.927	162.9	112.6	70.2	183.8	−0.50
668	JMP	9	71	345.1	+24.1	62.5	5.91	0.870	0.912	129.0	134.9	71.2	205.9	−0.17
669	CHP	7	71	3.3	+21.9	61.9	12.2	0.481	0.973	136.6	87.3	71.2	158.6	−0.35
670	JEP	7	70	344.5	+34.9	56.9	4.93	0.826	0.828	109.7	127.2	69.2	195.9	1.39
671	MCY	8	72	324.2	+31.6	56.8	11.0	1.013	0.907	107.7	183.6	71.5	253.9	1.65
681	OAQ	9	93	330.7	−4.3	63.2	28.5	0.374	0.996	161.7	286.3	92.4	17.3	−0.62
688 <sup>a</sup>	BTR	33	120	28.5	+37.8	63.0	4.05	0.936	0.772	136.3	145.5	120.8	265.0	0.47
691 <sup>a</sup>	ZCE	10	129	32.2	+8.8	73.5	<i>Inf.</i>	0.989	1.265	173.7	17.3	309.6	327.7	−2.70
694 <sup>a</sup>	OMG	33	164	116.1	+38.3	58.1	5.91	0.295	0.954	132.3	63.8	161.2	223.1	0.45
695 <sup>a</sup>	APA	11	146	95.6	+42.1	53.6	2.34	0.237	0.904	119.8	52.3	146.0	198.9	1.94
696	OAU	10	148	84.5	+48.0	62.1	7.75	0.617	0.977	128.3	102.7	147.8	250.4	0.94
705 <sup>a</sup>	UYL	14	169	111.7	+56.1	59.2	7.04	0.761	0.972	114.3	120.7	168.6	288.8	−0.23
713 <sup>a</sup>	CCR	8	181	125.6	+29.2	63.8	9.69	0.419	0.967	156.9	78.6	180.9	259.1	−0.36
715	ACL	5	183	77.1	+64.8	59.8	<i>Inf.</i>	0.964	1.061	109.8	201.3	189.6	31.4	−0.75
717	LAR	9	197	81.3	+39.8	65.4	<i>Inf.</i>	0.614	1.002	145.4	256.8	197.3	94.1	−0.85
718 <sup>a</sup>	XGM	33	206	96.9	+12.7	68.1	5.78	0.726	0.952	159.9	60.8	26.3	85.6	−0.69
719	LGM	11	232	106.8	+17.5	60.6	4.68	0.220	0.981	164.7	128.1	52.2	176.9	−0.01
727	ISR	10	275	231.5	+21.9	53.5	9.25	0.635	0.982	95.1	105.6	274.7	21.1	0.05
729 <sup>a</sup>	DCO	7	282	186.8	−16.4	71.8	<i>Inf.</i>	0.983	1.024	159.0	356.9	102.1	98.9	−1.29
731	ZBT	8	282	218.0	+8.5	64.8	5.70	0.711	0.947	134.5	115.2	281.3	35.7	−0.32
736 <sup>a</sup>	XIP	13	129	60.0	+33.4	66.3	8.97	0.605	0.991	153.5	100.9	128.8	231.8	−0.81
738 <sup>a</sup>	RER	24	137	44.8	−4.0	67.3	8.94	0.988	0.945	145.7	18.7	316.7	335.3	−0.71
739	LAR	11	155	28.4	+24.0	62.2	6.16	0.407	0.938	152.0	284.0	155.3	78.3	−0.02

<sup>a</sup> Shower confirmed in this work by also being detected in SonotaCo data.

**Table 3**Newly identified showers with median  $T_J < 2.0$  in prograde orbits.

IAU	Object	$N$	$\lambda_o$	R.A.	Dec.	$V_g$	$a$	$q$	$e$	$i$	$\omega$	Node	$\Pi$	$T_J$
427 <sup>a</sup>	FED	9	315	239.6	+62.4	35.1	18.6	0.971	0.975	54.7	194.3	315.1	149.3	0.84
643 <sup>a</sup>	KCN	10	287	136.5	+8.9	44.9	2.45	0.054	0.986	37.4	153.6	107.6	261.6	1.65
647 <sup>a</sup>	BCO	6	9	196.2	+24.9	27.3	10.9	0.689	0.945	22.3	248.9	11.1	259.5	1.35
653 <sup>a</sup>	RLY	46	32	280.4	+47.6	40.1	11.3	1.002	0.917	67.0	186.0	31.7	222.4	0.91
683	JTS	11	91	284.2	+1.5	36.9	17.0	0.389	0.984	35.9	283.5	89.3	13.1	0.84
701	BCE	5	153	325.4	+75.8	39.8	19.3	1.006	0.948	65.8	188.3	153.2	341.5	0.77
707	BPX	8	288	133.0	-36.3	45.7	93.3	0.746	0.992	73.1	59.6	107.7	167.6	0.36
708	RLM	15	293	148.6	+36.4	40.9	5.00	0.248	0.950	47.3	302.3	293.4	234.8	1.46
709 <sup>a</sup>	LCM	18	286	98.4	-31.5	25.4	4.85	0.833	0.826	33.2	48.5	105.8	155.1	1.98
714 <sup>a</sup>	RPI	7	177	22.8	+16.9	43.9	1.89	0.048	0.988	33.0	336.7	176.5	153.9	1.50
716	OCH	7	194	25.2	+43.7	40.8	7.15	0.364	0.949	55.2	288.1	193.4	120.7	1.13
720	NGB	6	244	211.3	+40.0	48.1	7.49	0.765	0.896	82.8	120.4	243.8	4.4	0.84
734	MOC	5	345	302.0	+49.1	29.9	4.87	0.890	0.815	45.9	141.3	345.3	127.4	1.85

<sup>a</sup> Shower confirmed in this work by also being detected in SonotaCo data.

The  $\kappa$ -Ursae Majorids (#445, KUM) are in the apex source, possibly also originating from a long period comet. The shower was discovered in 2011, when a CAMS-detected radiant concentration showed a strong correspondence in the SonotaCo network data for November 5, 2009 (Fig. 1B). It is likely that the shower was independently recognized in Japan. The 2009 shower may have been an outburst. The shower has since been detected annually in CAMS data at about the same level of activity.

The strong outburst of December  $\phi$ -Cassiopeiids (#446, DPC) in December of 2011 (Jenniskens, 2012) was also detected by the radar CMOR and has since been linked to Comet 3D/Biela (Wiegert et al., 2013). This Jupiter-family comet shower was also detected by SonotaCo (Fig. 1C). The agreement with the projected orbit of 3D/Biela for the return of 2010 is not good (Table 1). The comet now passes far from Earth's orbit in a lower-inclined orbit. The observed dust is thought to have been ejected long ago, when the inclination of the comet orbit was higher, some time prior to the discovery of the comet (Wiegert et al., 2013).

The February  $\varepsilon$ -Virginids (#506, FEV) are a late component of the Comae Berenicids (#20, COM), nominally active from  $\lambda_o = 252^\circ$  to  $302^\circ$ . The February  $\varepsilon$ -Virginids (#506, FEV) were assigned in the period  $\lambda_o = 300\text{--}328^\circ$  (Fig. 1D). At that time, the drift-corrected COM radiant would be at R.A. =  $205.4^\circ$ , Dec. =  $+12.4^\circ$ . The February  $\varepsilon$ -Virginids are found at a slightly lower right ascension (Steakley and Jenniskens, 2013). The stream is likely caused by the same Halley-type comet responsible for the Comae Berenicids.

Finally, the  $\upsilon$ -Andromedids (#507, UAN) are located near the radiant of early Perseids in the apex source (Holman and Jenniskens, 2013). They are weakly detected by SonotaCo (left panel of Fig. 2A). The shower is well separated from the established c-Andromedids (#411, CAN), which was discussed in Jenniskens et al. (2016a). The c-Andromedids are a strong shower in CAMS data (Fig. 2A).

### 3.2. Newly detected showers

Again in order of Working List shower number, the  $\kappa$ -Cancriids (#643, KCN) are active in the period defined by the solar longitude interval  $\lambda_o = 283\text{--}290^\circ$ . A compact string of radiants is surrounded by a more diffuse area of activity in CAMS data (Fig. 2B). SonotaCo shows what appears to be a string of radiants too, but not distributed in the same manner. The shower is located on the inside of the antihelion source, on the toroidal ring. These meteoroids have a small perihelion distance and short semi-major axis, similar to that of some sunskirter comets (Table 1). No parent body is known.

The January  $\lambda$ -Leonids (#644, JLL) appear to be a twin shower of the  $\kappa$ -Cancriids, possibly also having a denser central radiant area with a more diffuse region around it. Early in the activity period at  $\lambda_o = 269\text{--}288^\circ$ , the January  $\lambda$ -Leonids are diffuse in both CAMS and SonotaCo data. More recent CAMS data show that activity extends throughout the period of the  $\kappa$ -Cancriids.

The northern apex source  $\phi$ -Cancriids (#645, PHC) stand out well in CAMS data, but less clearly in the SonotaCo data (Fig. 2C). A group of ten meteors in SonotaCo data is centered on the CAMS-detected radiant. The shower is caused by a Halley type or long period comet in a retrograde orbit (Table 2).

The  $\beta$ -Comae Berenicids (#647, BCO) are located just above the antihelion source (Fig. 2D). They are due to an unknown prograde long period comet (Table 3).

The October  $\alpha$ -Virginids (#651, OAV) are a weak detection in the antihelion source of both CAMS and SonotaCo data (Fig. 3A). The meteors move in a typical Jupiter-family comet type orbit, but no parent body is known. The AOV are opposite to the ecliptic plane of the unconfirmed  $\mu$ -Virginids (#47, DLI).

The R-Lyrids (#653, RLY) are detected in the apex source of both CAMS and SonotaCo data (Fig. 3B). The source of the R-Lyrids is unknown. The nearby  $\varepsilon$ -Lyrids (#145, ELY) are from long period Comet C/1983 H1 (Iras-Araki-Alcock).

The April  $\phi$ -Capricornids (#655, APC) are an isolated grouping in the southern apex source of CAMS (Fig. 3C, Table 2). The sparser SonotaCo data during this time period cannot confirm the stream. Nearby showers also shown in Fig. 3C are the o-Serpentids (#652, OSP) and the  $\gamma$ -Sagittariids (#657, GSG). There is just a hint of the o-Serpentids in SonotaCo data, while the  $\gamma$ -Sagittariids (#750, SMV) are not detected.

The April  $\alpha$ -Antiliids (#656, AAA) are a group of slow meteors detected South-West of the antihelion source (Fig. 3D). The shower is active for only 9 days. At other times in the year, few meteors are detected from this area. SonotaCo does not have enough data in this time period to confirm the shower.

The May  $\beta$ -Cepheids (#658, MBE) form an elongated structure above the toroidal ring in the drift-corrected radiant map of CAMS data during late April (Fig. 4A). SonotaCo, too, finds a concentration of radiants around the median position of the CAMS-detected radiant. The shower is caused by an unknown Jupiter-family comet. The May  $\beta$ -Cepheids may well be late activity from the  $\lambda_o = 358\text{--}16^\circ$   $\phi$ -Draconids (#45, PDF), a previously confirmed shower (Jenniskens et al., 2016b). However, the May  $\beta$ -Cepheids are active one month later during  $\lambda_o = 37\text{--}48^\circ$ , and need a strong radiant drift unrelated to Earth's motion around the Sun to be in agreement.

The  $\varepsilon$ -Scorpiids (#660, EPS) are a southern hemisphere antihelion source shower. There is a tentative detection in SonotaCo data

**Table 4**  
Shower dispersion – data on shower duration in solar longitude ( $\lambda_o$ , °), the drift corrected radiant and speed's measurement accuracy ( $\pm$  = standard error, in ° or km/s) and dispersion ( $\sigma$  = one standard deviation, in ° or km/s), the drift rate of the apparent radiant ( $\Delta/\Delta\lambda_o$ ), the  $D_h$  threshold value, and the shower-to-background surface density ratio ( $S/B$ ).

IAU #	$\lambda_o$ Beg	$\lambda_o$ Peak	$\lambda_o$ End	$\Delta RA \pm$	$\Delta RA \sigma$	$\Delta Dec \pm$	$\Delta Dec \sigma$	$\Delta V_g \pm$	$\Delta V_g \sigma$	$\Delta RA/\Delta\lambda_o$	$\Delta Dec/\Delta\lambda_o$	$D_h$	$S/B$
427 <sup>a</sup>	314	315	316	0.3	0.8	0.2	0.6	0.3	0.9	+0.26	−0.20	0.15	150
445 <sup>a</sup>	221	225	228	0.2	0.4	0.3	0.9	0.3	0.8	+1.13	−0.34	0.10	6
446 <sup>a</sup>	246	252	258	0.4	3.2	0.2	1.5	0.1	1.1	+1.14	+0.37	0.06	19
506 <sup>a</sup>	300	314	328	0.2	1.8	0.2	1.3	0.2	1.4	+0.89	−0.37	0.14	7
507 <sup>a</sup>	87	96	104	0.5	2.9	0.3	1.7	0.3	1.4	+0.96	+0.39	0.20	15
643 <sup>a</sup>	283	287	290	0.5	1.6	0.3	1.0	1.1	3.5	+0.96	−0.29	0.19	8
644 <sup>a</sup>	269	288	295	0.6	2.9	0.3	1.5	0.6	3.0	+1.03	−0.31	0.18	6
645	188	190	198	0.4	1.1	0.5	1.5	0.4	1.1	+1.11	−0.20	0.20	4
647 <sup>a</sup>	4	9	15	0.8	1.8	0.5	1.3	0.4	1.0	+0.87	−0.38	0.10	5
651 <sup>a</sup>	15	16	21	0.4	1.0	0.1	0.4	0.4	1.0	+0.95	−0.37	0.10	2
652 <sup>a</sup>	15	18	20	0.4	1.3	0.5	1.6	1.0	3.1	+1.00	+0.03	0.18	4
653 <sup>a</sup>	14	32	56	1.0	6.8	0.7	4.4	0.3	2.3	+0.49	+0.07	0.08	8
655	25	32	40	0.5	1.4	0.8	2.6	1.7	5.5	+1.06	+0.28	0.08	5
656	25	31	34	2.0	4.9	0.8	2.0	0.4	0.9	+0.82	−0.37	0.11	5
657	30	30	33	0.8	2.0	0.9	2.3	0.5	1.2	+1.14	+0.00	0.25	2
658 <sup>a</sup>	37	41	48	3.3	14.2	0.7	3.1	0.3	1.5	+0.04	+0.27	0.15	4
660	46	49	52	0.3	0.7	0.3	0.7	1.1	2.7	+1.15	−0.12	0.15	2
664	42	46	55	3.0	11.3	1.7	6.4	0.3	1.0	+1.57	+0.01	0.10	4
667 <sup>a</sup>	67	70	75	0.3	1.5	0.5	2.0	0.3	1.3	+0.91	+0.40	0.20	12
668	68	71	74	0.3	0.9	0.4	1.1	0.3	1.0	+0.87	+0.39	0.18	14
669	69	71	73	0.6	1.6	0.5	1.4	0.5	1.4	+0.93	+0.40	0.18	7
670	67	70	72	0.6	1.5	0.7	1.9	0.5	1.4	+0.85	+0.38	0.18	5
671	68	72	73	0.6	1.8	0.6	1.8	0.3	0.8	+0.78	+0.32	0.18	5
680	82	85	87	0.6	1.8	0.3	0.8	0.7	2.0	+1.07	+0.27	0.15	16
681	87	93	99	0.3	1.0	0.1	0.3	0.2	0.5	+0.93	+0.35	0.10	7
683	84	91	93	0.3	1.0	0.3	0.9	0.6	2.1	+0.91	+0.10	0.15	5
684	86	89	92	0.2	0.5	0.4	0.9	0.5	1.2	+1.00	−0.02	0.07	2
688 <sup>a</sup>	117	120	124	0.3	1.9	0.3	1.9	0.2	1.0	+1.07	+0.35	0.13	11
689	117	121	126	0.3	1.0	0.3	1.2	0.2	0.9	+1.00	+0.27	0.07	7
691 <sup>a</sup>	125	129	135	0.5	1.7	0.3	0.9	1.8	5.8	+0.95	+0.34	0.15	3
692 <sup>a</sup>	134	138	142	0.4	2.0	0.3	1.5	0.1	0.7	+0.95	+0.26	0.07	22
694 <sup>a</sup>	151	164	168	0.4	2.2	0.3	1.9	0.2	1.3	+1.20	−0.18	0.15	8
695 <sup>a</sup>	142	146	151	1.5	4.9	0.5	1.7	0.6	2.0	+1.27	−0.04	0.20	5
696	145	148	151	0.6	1.9	0.5	1.6	0.5	1.4	+1.36	+0.03	0.15	2
701	152	153	154	0.6	1.4	0.2	0.4	0.2	0.5	+0.01	+0.33	0.10	10
703 <sup>a</sup>	154	157	162	1.2	4.1	0.8	2.8	0.3	0.9	+0.50	−0.24	0.10	5
705 <sup>a</sup>	165	169	174	0.4	1.5	0.3	1.1	0.5	1.7	+1.46	−0.15	0.15	9
706 <sup>a</sup>	165	172	184	0.6	2.1	0.4	1.4	0.6	2.4	+0.94	+0.37	0.15	7
707	285	288	293	0.8	2.1	0.9	2.4	0.5	1.5	+0.70	−0.27	0.15	3
708	286	293	296	0.4	1.5	0.1	0.6	0.3	1.2	+1.07	−0.34	0.10	9
709 <sup>a</sup>	279	286	295	0.5	2.2	0.7	3.0	0.3	1.1	+0.68	−0.06	0.13	9
710 <sup>a</sup>	307	317	321	0.4	1.8	0.3	1.3	0.6	2.5	+0.93	−0.39	0.18	7
712	335	339	344	0.3	0.8	0.3	0.7	0.6	1.3	+0.52	+0.13	0.16	2
713 <sup>a</sup>	177	181	185	0.3	0.9	0.2	0.6	0.2	0.6	+1.10	−0.24	0.13	4
714 <sup>a</sup>	171	177	183	0.9	2.4	0.5	1.3	1.4	3.7	+0.97	+0.37	0.15	5
715	188	183	194	0.9	2.0	0.3	0.6	0.3	0.7	+1.75	+0.08	0.11	11
716	187	194	197	0.6	1.6	0.4	1.0	0.6	1.7	+1.08	+0.36	0.15	3
717	195	197	202	0.7	2.1	0.3	0.8	0.6	1.7	+1.25	+0.06	0.10	2
718 <sup>a</sup>	200	206	218	0.4	2.4	0.3	2.0	1.3	7.6	+1.01	−0.05	0.10	3
719	226	232	234	0.3	0.8	0.7	2.2	0.4	1.4	+1.04	−0.12	0.13	5
720	243	244	248	0.7	1.7	0.7	1.7	0.6	1.4	+0.74	−0.34	0.21	4
724	266	268	270	0.8	1.9	0.4	0.9	0.2	0.5	+0.92	+0.40	0.08	4
726 <sup>a</sup>	263	268	272	0.3	1.1	0.2	0.7	0.2	0.7	+1.11	−0.05	0.05	5
727	273	275	281	0.6	1.8	0.2	0.8	0.4	1.2	+0.79	−0.25	0.20	5
729 <sup>a</sup>	280	282	286	0.2	0.6	0.5	1.3	0.6	1.7	+0.93	−0.39	0.10	1
731	278	282	289	0.8	2.2	0.3	1.0	1.1	3.1	+0.88	−0.31	0.14	2
732	335	338	345	0.8	3.0	0.4	1.5	0.9	3.4	+0.92	−0.39	0.25	4
733	333	343	344	1.0	2.8	1.1	3.2	0.4	1.2	+1.02	−0.33	0.06	2
734	345	345	349	2.4	5.3	0.3	0.6	0.7	1.6	+0.53	+0.21	0.14	4
736 <sup>a</sup>	120	129	140	0.6	2.3	0.4	1.5	0.3	1.2	+1.15	+0.20	0.15	1
738 <sup>a</sup>	127	137	149	0.2	1.2	0.3	1.6	0.7	3.5	+0.90	+0.28	0.13	3
739	150	155	157	0.4	1.4	0.4	1.3	0.2	0.7	+1.00	+0.35	0.13	3
746 <sup>a</sup>	244	252	257	1.0	2.9	0.5	1.5	0.5	1.6	+0.62	−0.26	0.15	14
749 <sup>a</sup>	303	339	320	0.6	2.3	0.4	1.5	0.4	1.6	+1.10	−0.35	0.25	5
750 <sup>a</sup>	337	344	350	0.7	2.5	0.4	1.5	1.0	3.5	+0.93	−0.39	0.25	7

<sup>a</sup> Shower confirmed in this work by also being detected in SonotaCo data.

(Fig. 4B). The shower has a relatively low  $q = 0.127$  AU perihelion distance and no known parent body.

The May  $\xi$ -Aurigids (#664, MXA) are a high declination shower, well isolated from the apex source (Fig. 4C), with an unusually

small longitude of perihelion. This shower needs confirmation from a separate survey. They resemble the April  $\psi$ -Ursae Majorids (#133, PUM), but are active 23° later in solar longitude and require an unusual radiant drift if they are the same.

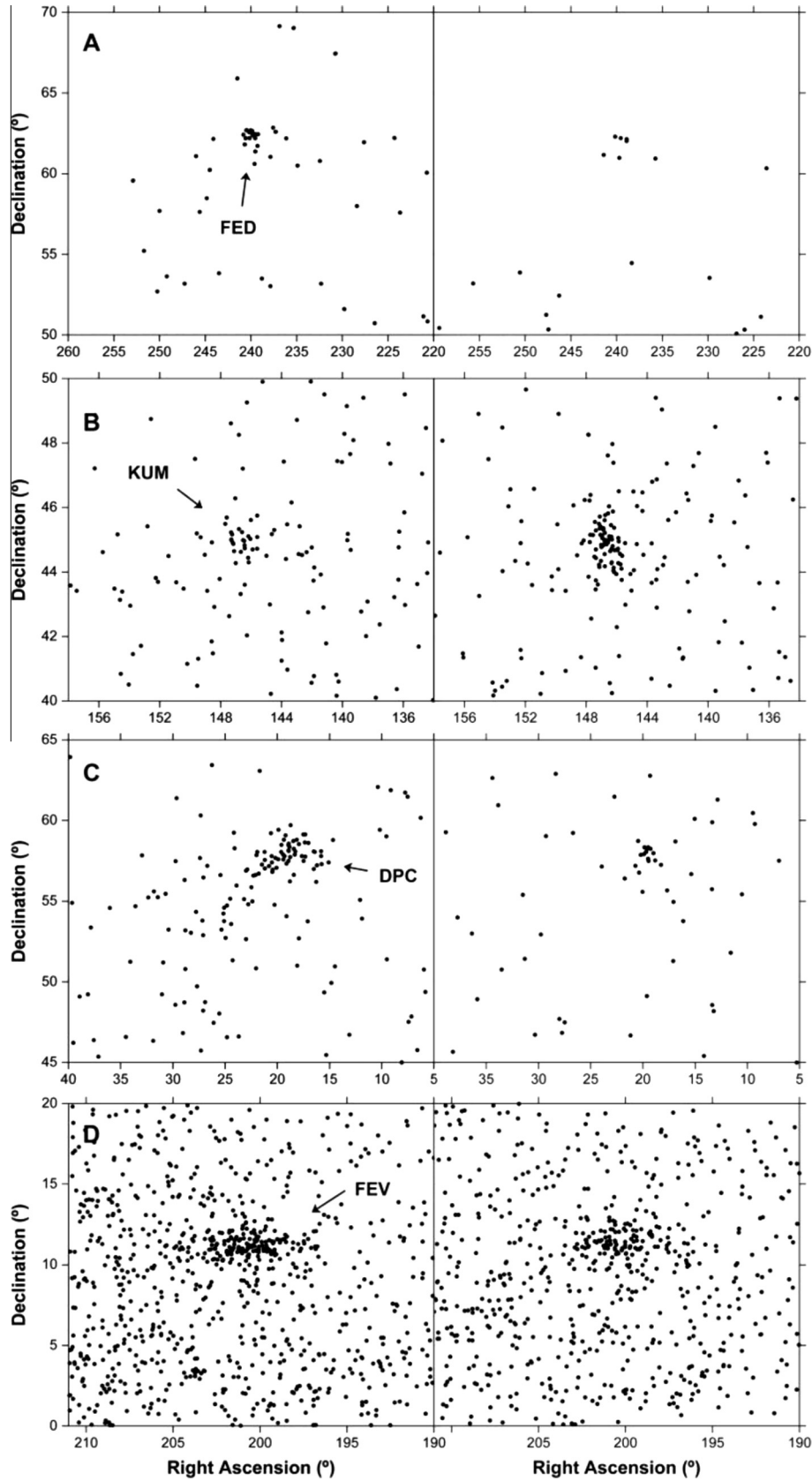


**Fig. 1.** The following diagrams show the drift-corrected equatorial coordinates of the direction from which meteoroids approach us after removing the effects of Earth's gravity and spin. The left diagram shows 2010–2015 CAMS data, the right diagram shows 2007–2013 SonotaCo data, both drift corrected to the solar longitude ( $\lambda_o$ ) listed for that shower in Tables 1–3. From top to bottom: (A) the February  $\eta$ -Draconids (#427, FED) – Period  $\lambda_o = 314$ – $316^\circ$ ; (B) the  $\kappa$ -Ursae Majorids (#445, KUM) – Period  $\lambda_o = 221$ – $228^\circ$ ; (C) the December  $\phi$ -Cassiopeiids (#446, DPC) – Period  $\lambda_o = 246$ – $258^\circ$ ; (D) the February  $\eta$ -Virginids (#506, FEV) – Period  $\lambda_o = 300$ – $328^\circ$ .

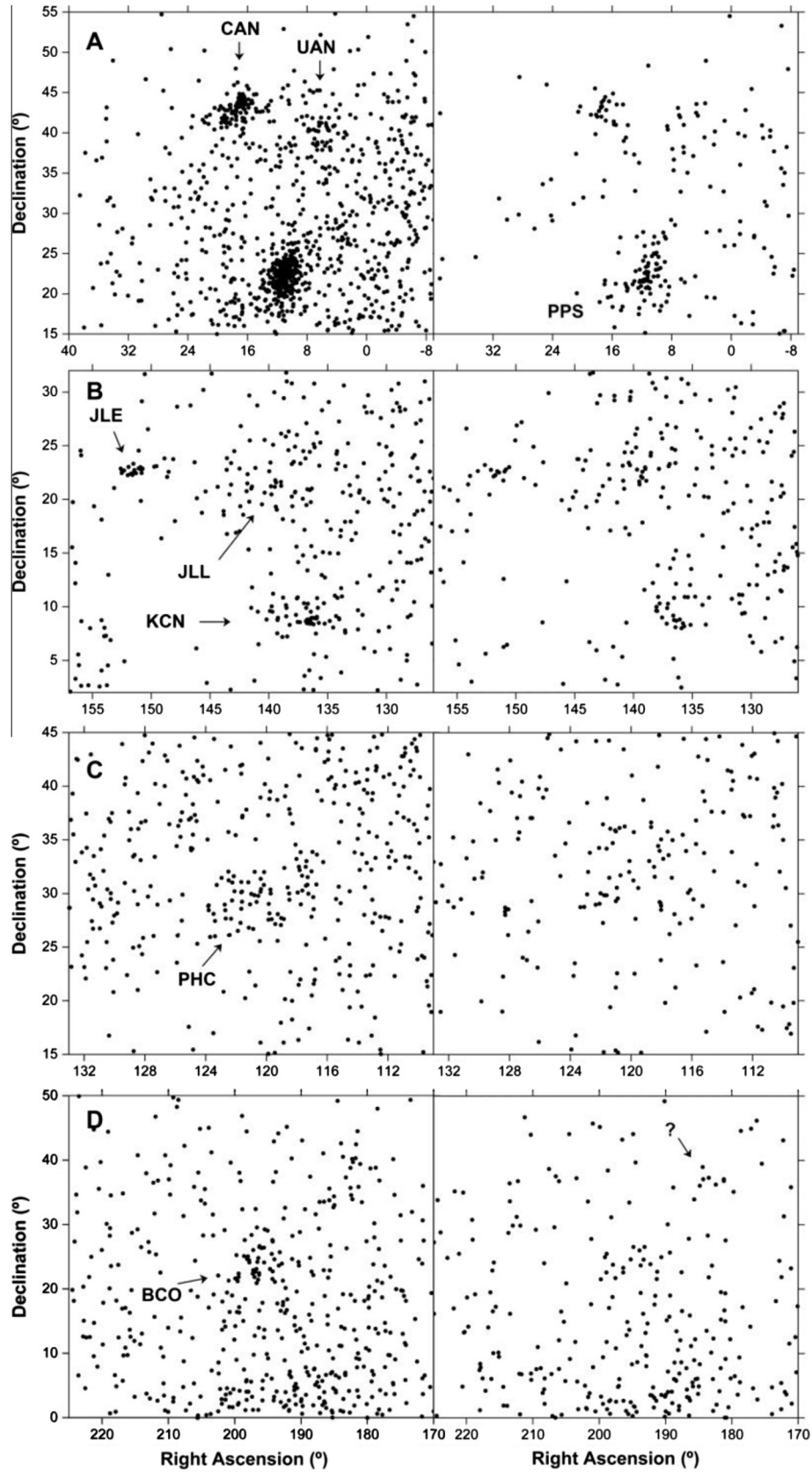


**Fig. 2.** As Fig. 1: (A) the  $\nu$ -Andromedids (#507, UAN) – Period  $\lambda_o = 93\text{--}102^\circ$ . Also shown are the c-Andromedids (#411, CAN) and  $\phi$ -Piscids (#372, PPS); (B) the  $\kappa$ -Cancrids (#643, KCN) and the January  $\lambda$ -Leonids (#644, JLL) – Period  $\lambda_o = 283\text{--}290^\circ$  (drift corrected to  $287^\circ$ ). Also shown are the January Leonids (#319, JLE); (C) the  $\phi$ -Cancrids (#645, PHC) – Period  $\lambda_o = 188\text{--}190^\circ$ ; (D) the  $\beta$ -Comae Berenicids (#647, BCO) – Period  $\lambda_o = 4\text{--}15^\circ$ .

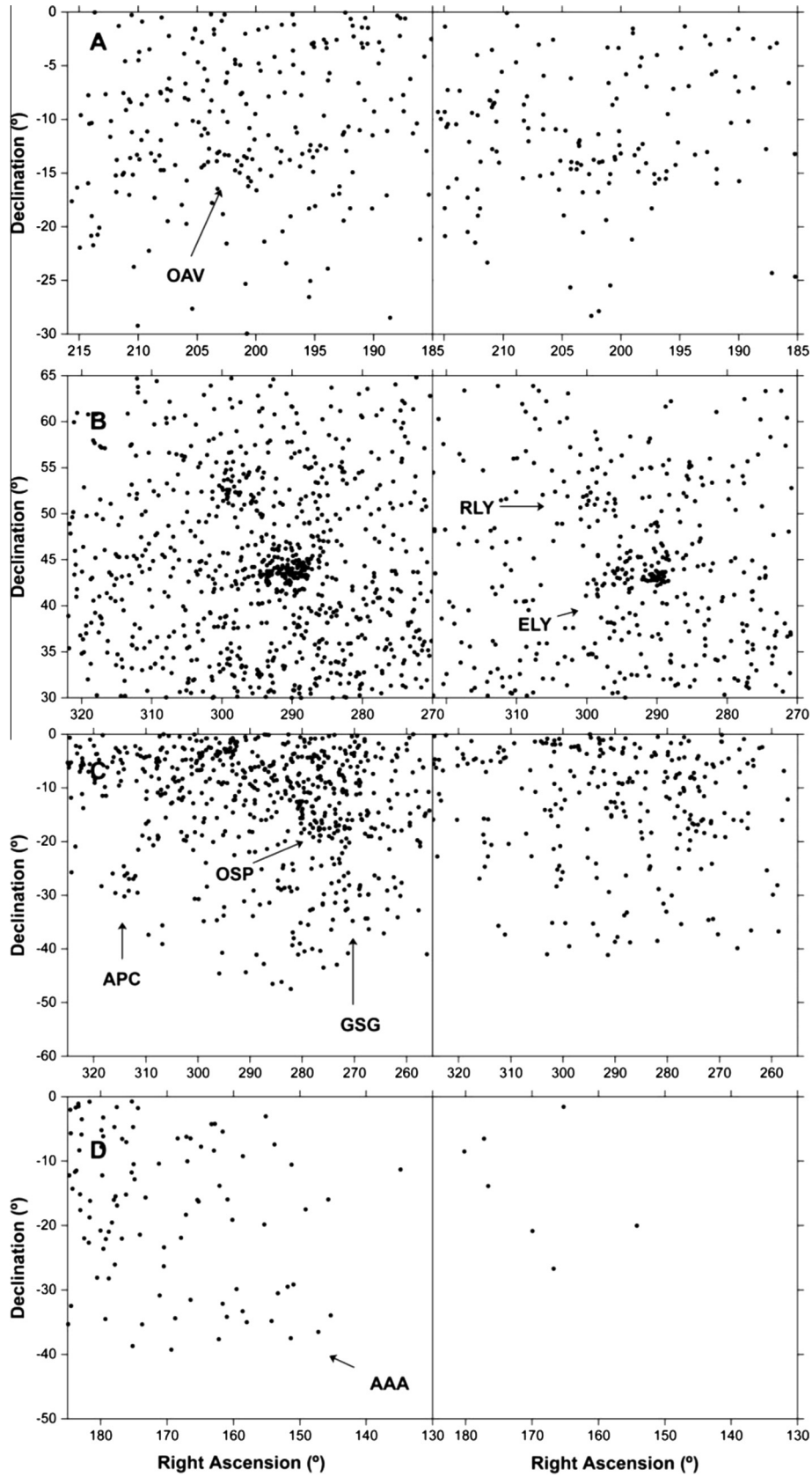


**Fig. 3.** As Fig. 1: (A) the October  $\alpha$ -Virgins (#651, OAV) – Period  $\lambda_o = 15\text{--}21^\circ$ ; (B) the R-Lyrids (#653, RLY) – Period  $\lambda_o = 37\text{--}55^\circ$  (drift corrected to  $50^\circ$ ). Also shown are the  $\eta$ -Lyrids (#145, ELY); (C) the o-Serpentids (#652, OSP), the April  $\phi$ -Capricornids (#655, APC), and the  $\gamma$ -Sagittariids (#657, GSG) – Period  $\lambda_o = 25\text{--}40^\circ$  (drift corrected to  $32^\circ$ ); (D) the April  $\alpha$ -Antiliids (#656, AAA) – Period  $\lambda_o = 25\text{--}34^\circ$ .

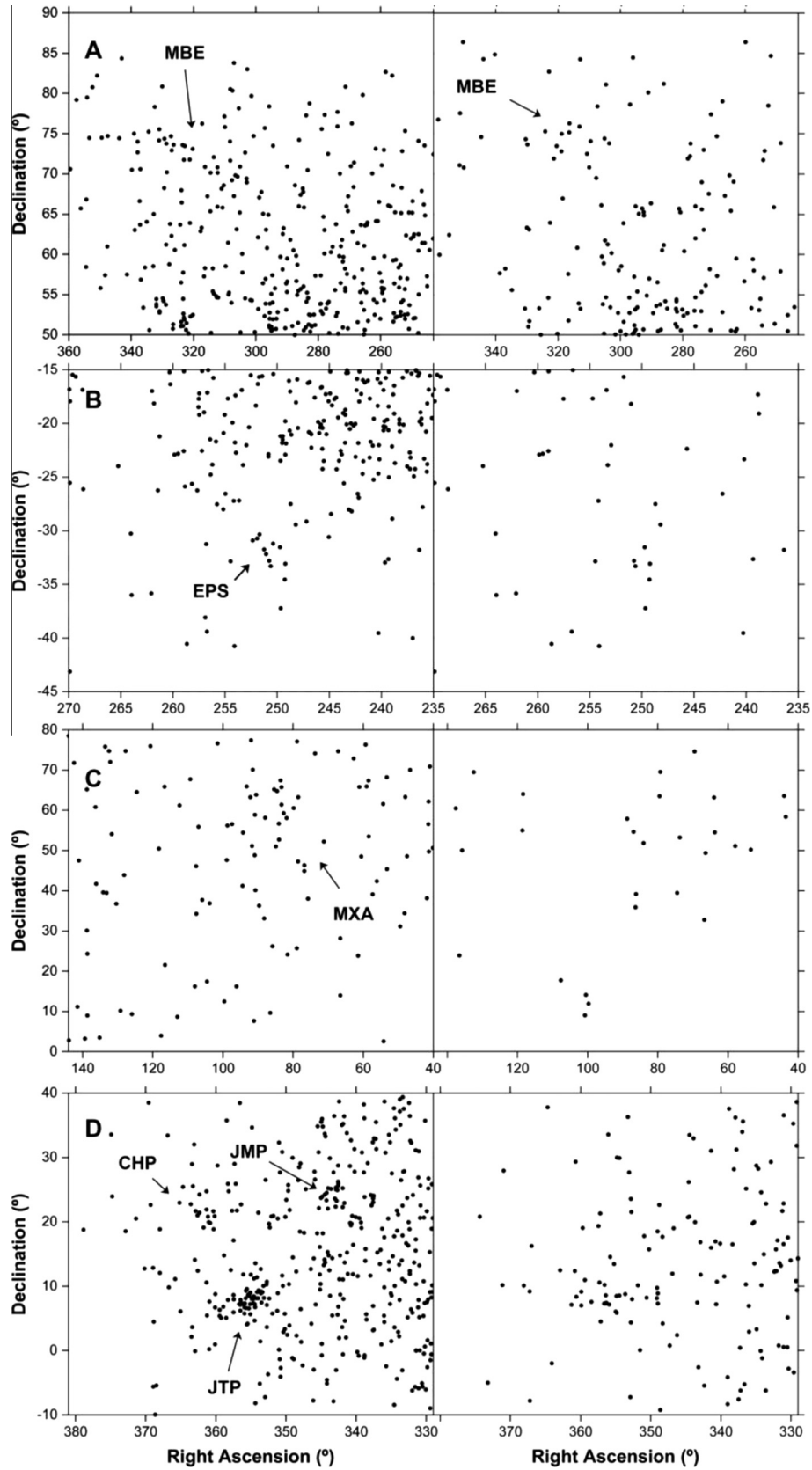


**Fig. 4.** As Fig. 1: (A) the May  $\beta$ -Cepheids (#658, MBE) – Period  $\lambda_0 = 37\text{--}48^\circ$ ; (B) the  $\epsilon$ -Scorpiids (#660, EPS) – Period  $\lambda_0 = 46\text{--}52^\circ$ ; (C) the May  $\xi$ -Aurigids (#664, MXA) – Period  $\lambda_0 = 42\text{--}55^\circ$ ; (D) the June  $\theta$ -Piscids (#667, JTP), the June  $\mu$ -Pegasus (#668, JMP), and the  $\xi$ -Pegasus (#669, CHP) – Period  $\lambda_0 = 67\text{--}75^\circ$ .

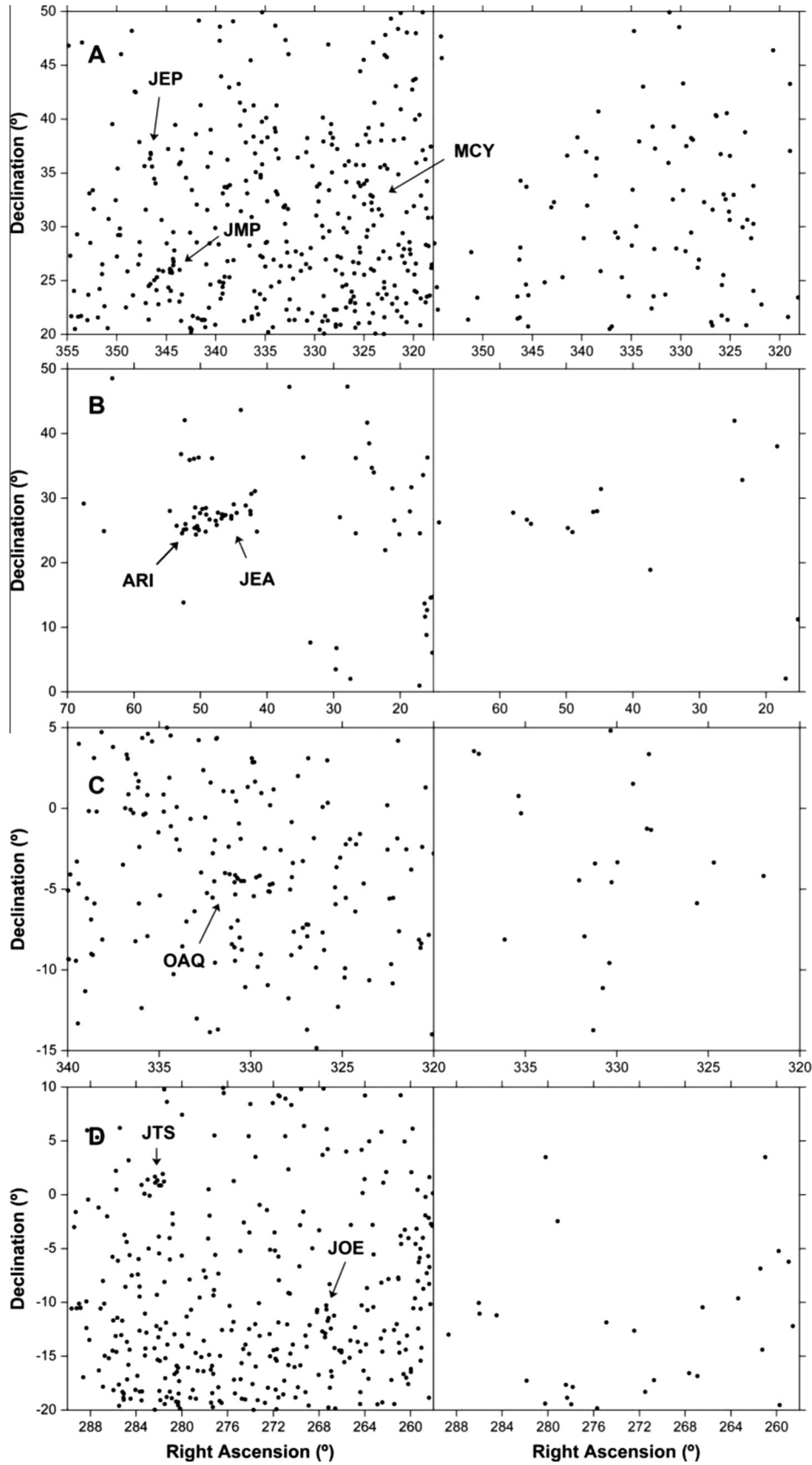


**Fig. 5.** As Fig. 1: (A) the only tentatively detected June  $\eta$ -Pegasids (#670, JEP) and  $\mu$ -Cygnids (#671, MCY) – Period  $\lambda_0 = 67-78^\circ$ . Also shown are the June  $\mu$ -Pegasids (#668, JMP); (B) the June  $\varepsilon$ -Arietids (#680, JEA) – Period  $\lambda_0 = 82-87^\circ$ . Also shown are the Daytime Arietids (#171, ARI); (C) the o-Aquariids (#681, OAQ) – Period  $\lambda_0 = 87-99^\circ$ ; (D) the June  $\theta$ -Serpentids (#683, JTS) and only tentatively detected June o-Serpentids (#684, JOE) – Period  $\lambda_0 = 86-92^\circ$  (drift corrected to  $89^\circ$ ).

The June  $\theta$ -Piscids (#667, JTP) are a strong northern apex source shower in CAMS data and are also detected by SonotaCo (Fig. 4D). The shower is caused by a retrograde long period or Halley-type comet. Two other nearby showers are also visible in CAMS data, the June  $\mu$ -Pegasids (#668, JMP) and the  $\chi$ -Pegasids (#669, CHP). These are not confirmed by SonotaCo, perhaps because of insufficient observations. Both are likely from retrograde-moving long period comets.

Fig. 4D also contains the  $\xi$ -Pegasids (#669, CHP), a well-defined group in CAMS data, but not confirmed by SonotaCo. This shower is also caused by an unknown long period comet.

The tentatively detected June  $\eta$ -Pegasids (#670, JEP) are a small compact group of radiants still recognized in the more recent dataset, but in need of validation. The weak nearby  $\mu$ -Cygnids (#671, MCY) are perhaps also detected as a weak group in SonotaCo data (Fig. 5A).

The June  $\varepsilon$ -Arietids (#680, JEA) are a component of the Daytime Arietids (#171, ARI), slightly displaced to higher declination (Fig. 5B). They are likely related to the Marsden sunskirter group responsible for the Daytime Arietids.

The  $\sigma$ -Aquiriids (#681, OAQ) were detected as a string of radiants (Fig. 5C). The string itself spreads parallel to the ecliptic plane evenly over the period  $\lambda_o = 87\text{--}96^\circ$ . The ecliptic plane is at Dec.  $= -12^\circ$ , arguing against measurement error. The more sparse SonotaCo data in this time period did not detect this possible shower in the southern apex source.

The June  $\theta$ -Serpentids (#683, JTS) are a compact shower, above and well isolated from the antihelion source (Fig. 5D). This shower is caused by an unidentified long period comet. The June  $\sigma$ -Serpentids (#684, JOE) are in the antihelion source (Table 1) and are a more uncertain identification (Fig. 5D). There is no SonotaCo data to evaluate the reliability of these detections.

The  $\beta$ -Triangulids (#688, BTR) are a diffuse shower in the apex source active in the period  $\lambda_o = 117\text{--}124$ . The shower is located north of, and active late in the season of, the  $\phi$ -Piscids (#372, PPS) (Fig. 6A). The 49 Andromedids (#549, FAN) are just to the north. The source is likely an unknown Halley-type comet.

The  $\tau$ -Capricornids (#689, TAC) are a weak detection in the antihelion source of CAMS (Fig. 6B), but the shower is not recognized in the more sparse SonotaCo data (Fig. 6B). It is possible that this shower is transient.

The  $\zeta$ -Cetids (#691, ZCE) are a weak detection in the southern apex source of both CAMS and SonotaCo, just above the  $\eta$ -Eridanids (#191, ERI) shower (Fig. 6C). A long period comet is responsible.

The  $\varepsilon$ -Aquiriids (#692, EAQ) are late  $\alpha$ -Capricornids (#1, CAP) in the antihelion source. They were discussed before (Jenniskens et al., 2016a). They are detected both by SonotaCo and CAMS. The August  $\sigma$ -Geminids (#694, OMG) are a strong apex source shower in both CAMS and SonotaCo data (Fig. 6D). The shower is caused by a long period or Halley-type comet. Also shown are the Aurigids (#206, AUR) of long period Comet C/1911 N1 (Kiess).

The August  $\psi$ -Aurigids (#695, APA) are at the same position as the August  $\sigma$ -Geminids, but earlier in time (Fig. 7A). The APA are exceptional in having a Jupiter-family comet like semi-major axis, but move in a retrograde orbit. The APA are detected  $\lambda_o = 142\text{--}151$ , the August  $\sigma$ -Geminids (#694, OMG) during  $\lambda_o = 151\text{--}168^\circ$ . This may be the same shower. The weak  $\sigma$ -Aurigids (#696, OAU) are an apex source shower that originated likely from a long period comet. They are not confirmed by the sparse SonotaCo data during this time (Fig. 7B).

The  $\beta$ -Cepheids (#701, BCE) is a compact high-declination shower in a prograde long period comet type orbit (Fig. 7B). The shower is active for a very short period of time. The CAMS-detected sample has most meteors in the period  $\lambda_o = 152.96\text{--}153.29^\circ$  and a group at  $153.72\text{--}153.93^\circ$ . The shower is not detected in the SonotaCo data, suggesting transient activity.

The high declination  $\iota$ -Draconids (#703, IOD) are a component to the Jupiter-family comet type kappa Cygnid complex (Jenniskens et al., 2016a). The shower is shown here to demonstrate how well it appears in both current CAMS and SonotaCo data sets (Fig. 7C).

The UY-Lyncids (#705, UYL) are a strong apex source in CAMS and SonotaCo meteoroid orbit database, each containing similar amounts of orbits (Fig. 6D). The shower is caused by a Halley type or long period comet.

The  $\zeta$ -Piscids (#706, ZPI) are an antihelion source shower on the toroidal ring, with low perihelion distance orbits. The SonotaCo detection is tentative, possibly because the dataset is more sparse (Fig. 7D).

The  $\beta$ -Pyxidids (#707, BPX) appear to be a section of the southern toroidal ring, but the meteors have a long period comet type orbit (Table 3). SonotaCo detected the shower only tentatively (Fig. 8A).

The nearby  $\lambda$ -Canis Majorids (#709, LCM) are a strong southern hemisphere shower south of the antihelion (Fig. 8B). This shower has a strong detection in SonotaCo data also. The shower may be caused by a Halley-type comet in a prograde orbit (Table 3).

The R-Leonids Minorids (#708, RLM) are on the toroidal ring, just north of the antihelion source, and may be a transient shower. The shower is strong in CAMS data, but not observed in SonotaCo data (Fig. 8B). The narrow dispersion in declination also points to a transient nature.

The  $\iota$ -Leonids (#710, IOL) are an antihelion source shower on the toroidal ring. Meteoroid orbits have a short  $q = 0.050$  AU perihelion distance, significant inclination and high eccentricity (Table 1). The shower has a high Tisserand parameter. Both detections in CAMS and SonotaCo are strong (Fig. 8C).

The February  $\delta$ -Cygnids (#712, FDC) are tentatively identified from a faint grouping in CAMS data on the toroidal ring, typical of other such showers (semi-major axis  $a \sim 6$  AU, inclination  $i \sim 55^\circ$ ), but with no corroboration from sparse SonotaCo data (Fig. 8D).

The  $\chi$ -Cancrids (#713, CCR) are a weak apex source shower also detected by SonotaCo. A long period comet is likely responsible (Fig. 9A).

The  $\rho$ -Piscids (#714, RPI) are a low  $q = 0.048$  AU shower on the inside of the antihelion source on the toroidal ring. The SonotaCo detection is weak or absent, possibly due to lack of data in this time period (Fig. 7D).

The  $\alpha$ -Camelopardalids (#715, ACL) are a compact shower clearly detected in CAMS, but not in SonotaCo. This high declination long period comet shower is likely transient (Fig. 9B).

The October  $\chi$ -Andromedids (#716, OCH) are a weak shower on the toroidal ring, not corroborated by the more sparse SonotaCo data (Fig. 9C). Orbital elements are typical for others in the nearby ring (Table 3).

The  $\lambda$ -Aurigids (#717, LAU) are a weak apex source meteor shower. SonotaCo has a similar amount of data and also contains a weak detection (Fig. 9D). Orbital elements are those of a long period comet. The next showers, #718 and #719, were previously discussed in Jenniskens et al. (2016a).

The November  $\gamma$ -Bootids (#720, NGB) are isolated from the apex source, perhaps confirmed with just a triplet of meteors from the SonotaCo database (Fig. 10A). The shower may be caused by a long period or Halley-type comet.

The  $\lambda$ -Piscids (#724, LAP) are an isolated compact shower, not detected by SonotaCo, possibly a meteor outburst from a Jupiter-family type comet shower (Fig. 10B). In addition to those extracted, there are potentially 4 extra members with a measured geocentric speed  $V_g = 0$  km/s, meaning that the measured speed (with a significant error bar) was below the escape speed from Earth. Shower #726 is discussed in Jenniskens et al. (2016a).

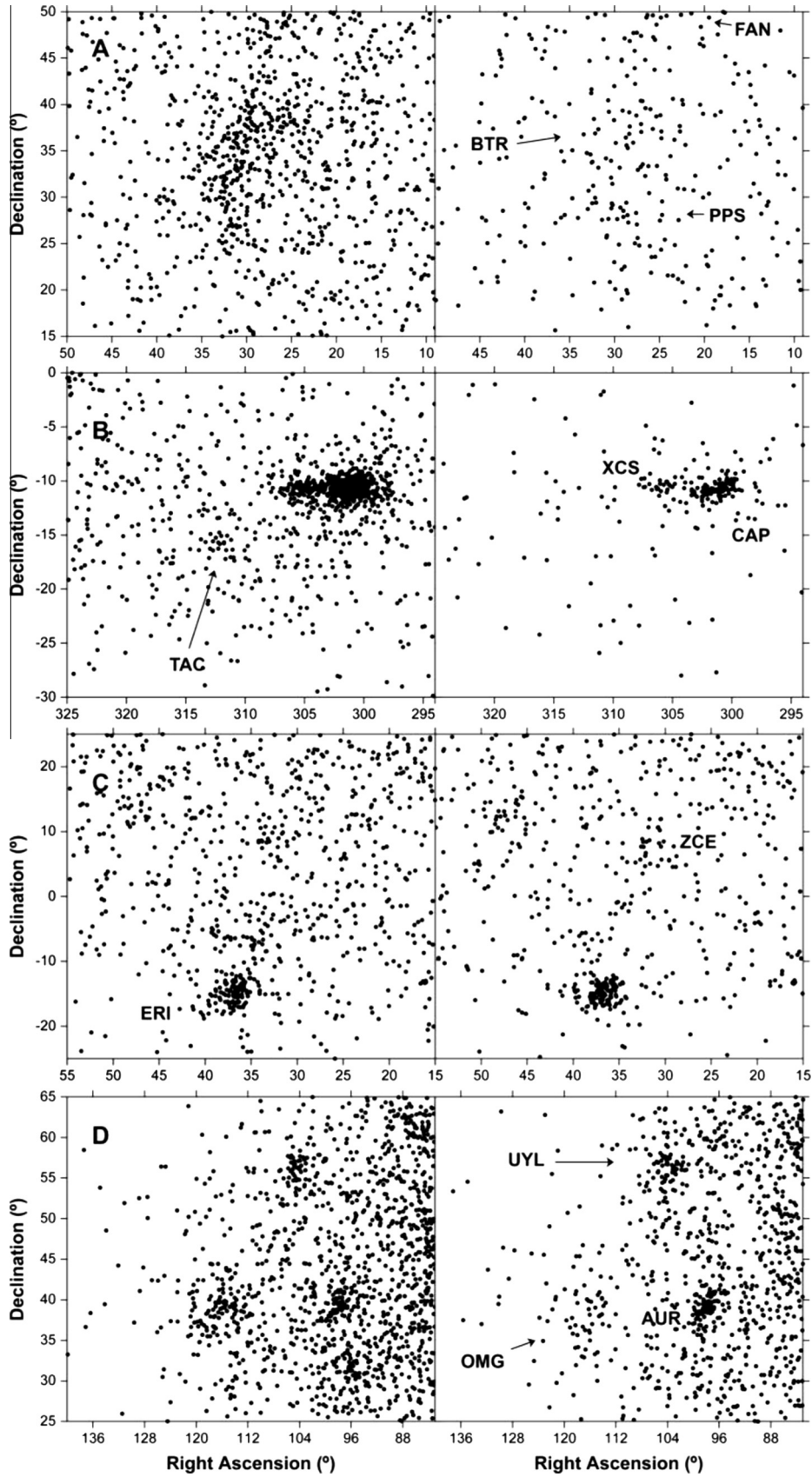


**Fig. 6.** As Fig. 1: (A) the  $\beta$ -Triangulids (#688, BTR) – Period  $\lambda_o = 117-124^\circ$ . Also shown are the  $\phi$ -Piscids (#372, PPS) and 49 Andromedids (#549, FAN); (B) the  $\tau$ -Capricornids (#689, TAC) – Period  $\lambda_o = 117-126^\circ$ ; (C) the  $\zeta$ -Cetids (#691, ZCE) – Period  $\lambda_o = 125-135^\circ$ ; (D) the August  $\alpha$ -Geminids (#694, OMG) and UY-Lyncids (#705, UYL) – Period  $\lambda_o = 151-174^\circ$  (drift corrected to  $164^\circ$ ). Also shown are the Aurigids (#206, AUR).

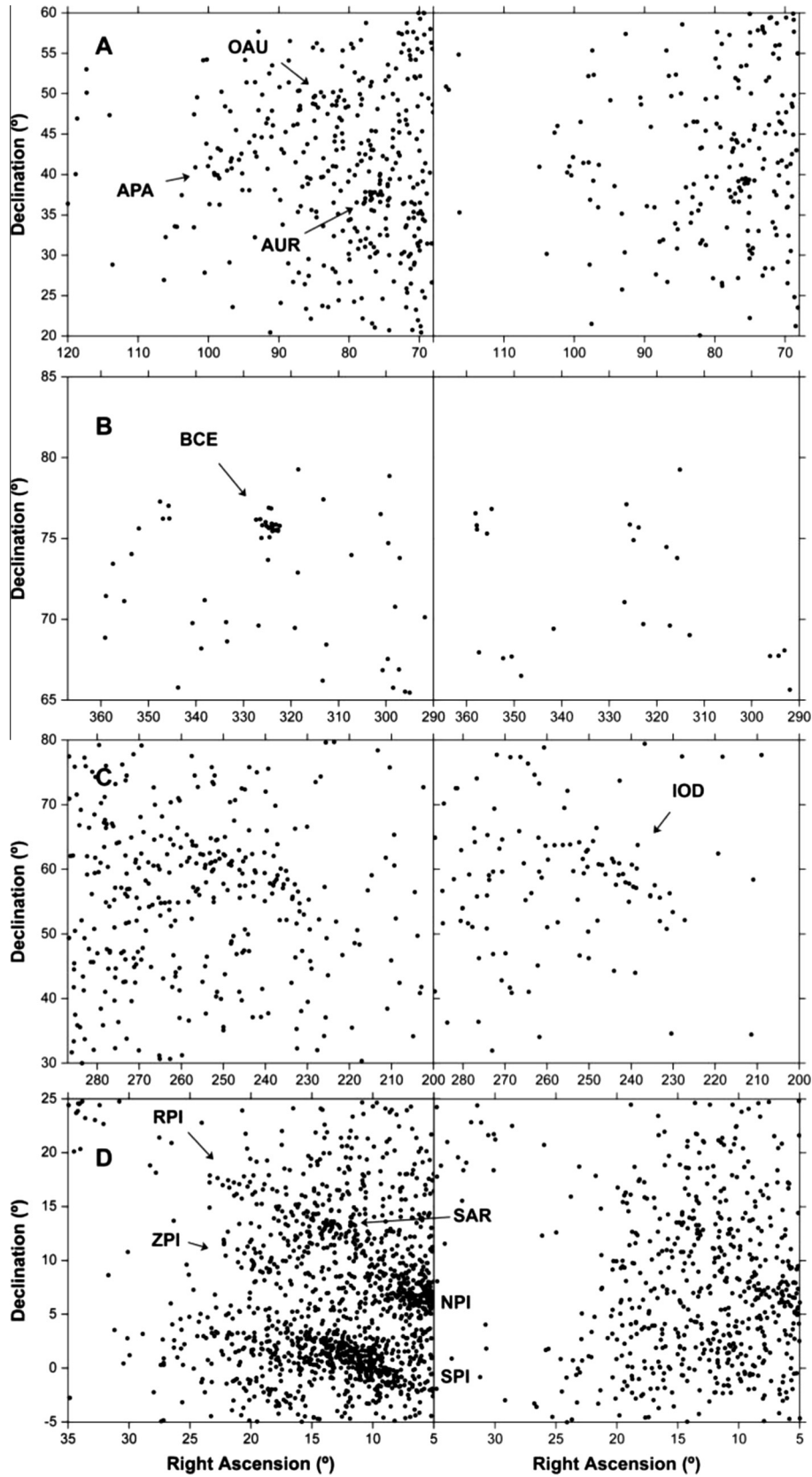


**Fig. 7.** As Fig. 1: (A) the August  $\psi$ -Aurigids (#695, APA) and the nearby o-Aurigids (#696, OAU) – Period  $\lambda_o = 142\text{--}151^\circ$  (drift corrected to  $146^\circ$ ). Also shown are the Aurigids; (B) the  $\beta$ -Cepheids (#701, BCE) – Period  $\lambda_o = 152\text{--}154^\circ$ ; (C) the  $\iota$ -Draconids (#703, IOD) – Period  $\lambda_o = 154\text{--}162^\circ$ ; (D) the  $\zeta$ -Piscids (#706, ZPI) and the  $\rho$ -Piscids (#714, RPI) – Period  $\lambda_o = 165\text{--}184^\circ$ . Also shown are the September  $\mu$ -Arietids (#219, SAR) and the Taurid Complex showers Northern  $\delta$ -Piscids (#215, NPI) and Southern  $\delta$ -Piscids (#216, SPI).

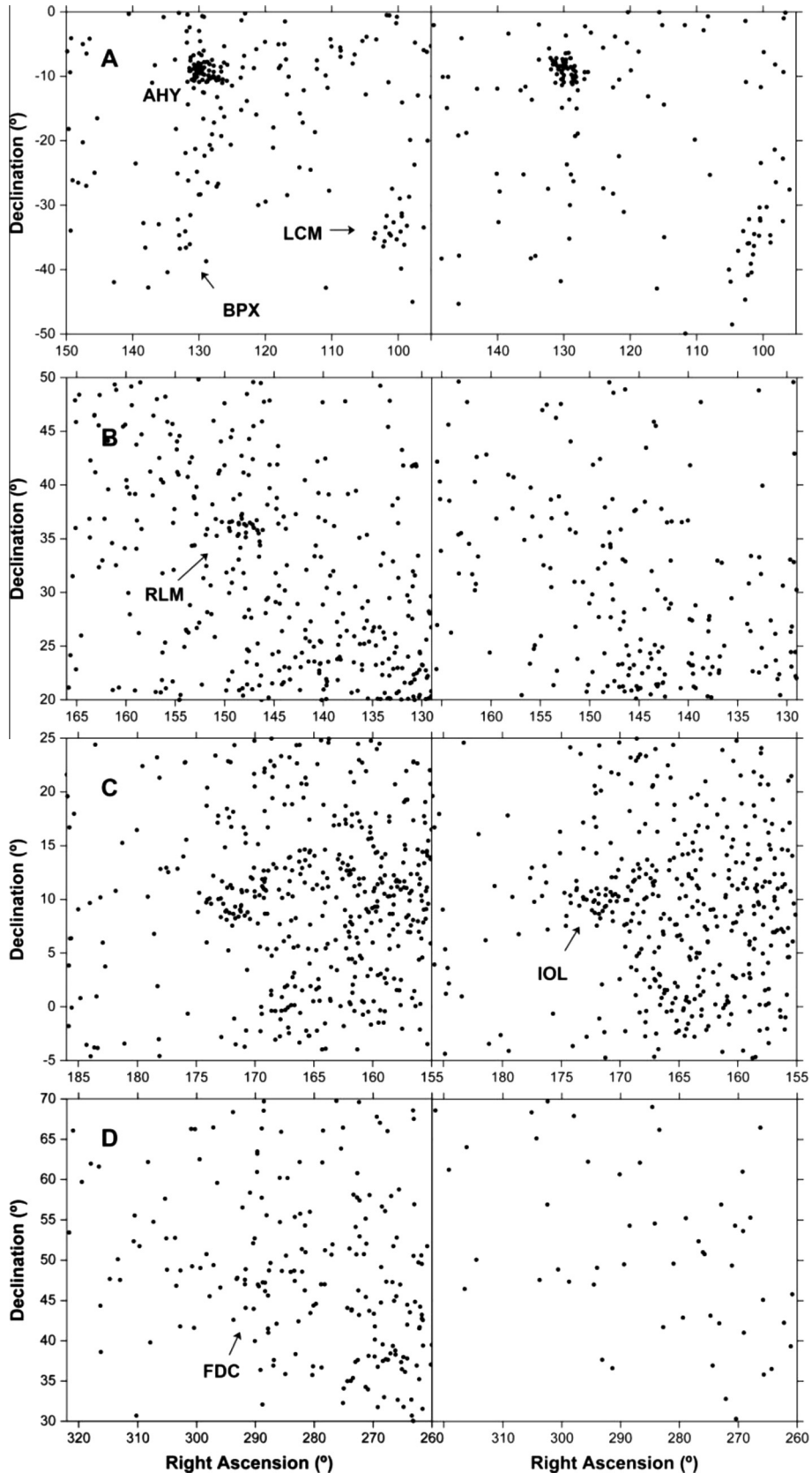


**Fig. 8.** As Fig. 1: (A) the  $\beta$ -Pyxidids (#707, BPX) and the  $\lambda$ -Canis Majorids (#709, LCM) – Period  $\lambda_o = 279\text{--}295$  (drift corrected to  $286^\circ$ ). Also shown are the  $\alpha$ -Hydrids (#331, AHY); (B) the R-Leonis Minorids (#708, RLM) – Period  $\lambda_o = 286\text{--}296^\circ$ ; (C) the  $\tau$ -Leonids (#710, IOL) – Period  $\lambda_o = 307\text{--}321^\circ$ ; (D) the only tentatively detected February  $\delta$ -Cygnids (#712, FDC) – Period  $\lambda_o = 335\text{--}344^\circ$ .

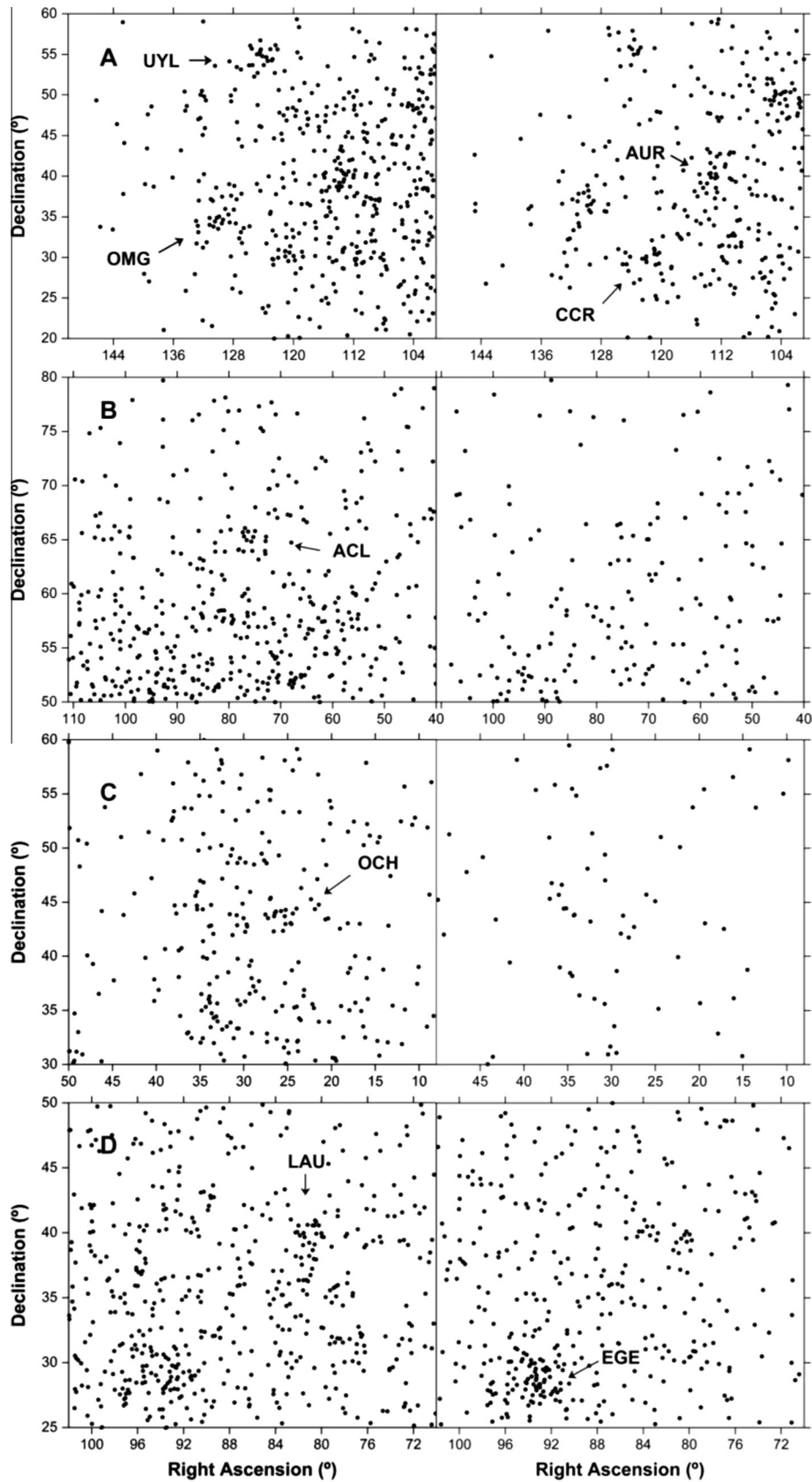


**Fig. 9.** As Fig. 1: (A) the  $\chi$ -Cancerids (#713, CCR) – Period  $\lambda_o = 171\text{--}183^\circ$  (drift corrected to  $177^\circ$ ); (B) the  $\alpha$ -Camelopardalids (#715, ACL) – Period  $\lambda_o = 188\text{--}194^\circ$ ; (C) the October  $\chi$ -Andromedids (#716, OCH) – Period  $\lambda_o = 187\text{--}197^\circ$ ; (D) the  $\lambda$ -Aurigids (#717, LAU) – Period  $\lambda_o = 195\text{--}202^\circ$ . Also shown are the  $\varepsilon$ -Geminids (#23, EGE).

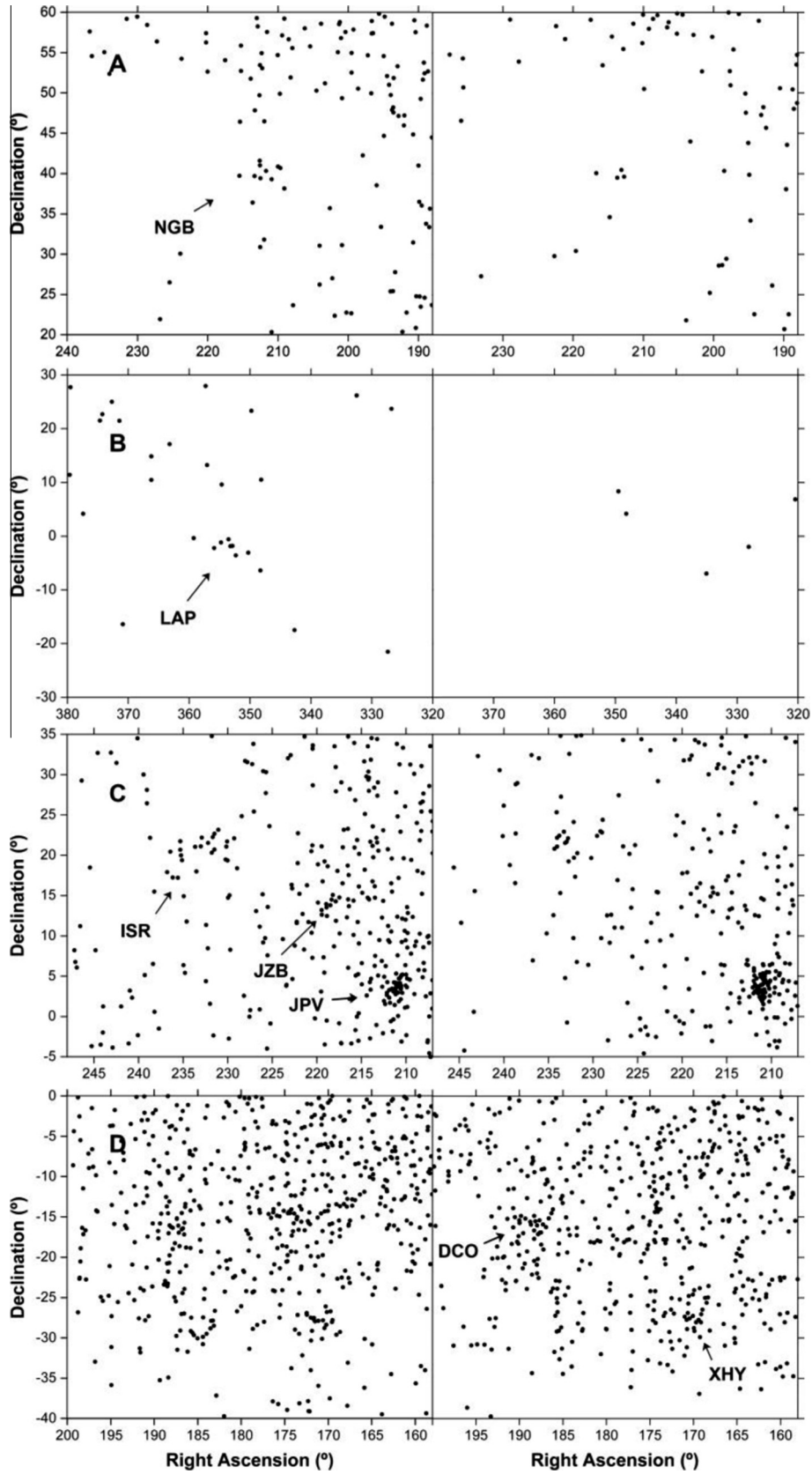


**Fig. 10.** As Fig. 1: (A) the November  $\gamma$ -Bootids (#720, NGB) – Period  $\lambda_o = 243\text{--}248^\circ$ ; (B) the  $\lambda$ -Piscids (#724, LAP) – Period  $\lambda_o = 266\text{--}270^\circ$ ; (C) the  $\tau$ -Serpentids (#727, ISR) and  $\zeta$ -Bootids (#731, JZB) – Period  $\lambda_o = 273\text{--}281^\circ$ ; (D)  $\delta$ -Corvids (#729, DCO) – Period  $\lambda_o = 280\text{--}286^\circ$ . Also shown are the  $\xi$ -Hydrids (#567, XHY).

The  $\iota$ -Serpentids (#727, ISR) are well detected in both CAMS and SonotaCo data (Fig. 10C). This apex shower is likely caused by a high inclination long period comet.

The  $\delta$ -Corvids (#729, DCO) are part of the southern apex source. They are a strong detection in SonotaCo data and more difficult to isolate from the background in CAMS (Fig. 10D). The shower is caused by a long period comet.

The  $\zeta$ -Bootids (#731, JZB) are a weak long period comet shower, only tentatively detected by SonotaCo (Fig. 10C).

The February  $\gamma$ -Virginids (#732, FGV) are a very compact shower with the lowest perihelion distance  $q = 0.018$  AU on record (Table 1). The shower is not detected by SonotaCo, perhaps because it is transient (Fig. 11A).

The  $\lambda$ -Leonids (#733, LAL) are a Jupiter-family type shower, only a weak group in the antihelion source. Three close orbits are detected in SonotaCo data (Fig. 11B).

The March  $\alpha$ -Cygids (#734, MOC) are a compact toroidal ring shower, not detected by SonotaCo (Fig. 11C). This shower may be transient as well.

The March  $\xi$ -Perseids (#736, XIP) are an apex source long period comet shower active during the Perseid season. The meteors appear in the early morning from a direction on the day-side of the apex source. SonotaCo has a more defined detection than CAMS (Fig. 11D).

The March  $\rho$ -Eridanids (#738, RER) are a diffuse radiant just above the  $\eta$ -Eridanids (#191, ERI) (Fig. 12A). This shower is discussed in Jenniskens et al. (2016a). SonotaCo observations are more sparse, but can confirm the detection.

The  $\lambda$ -Arietids (#739, LAR) are an apex shower from a long period or Halley-type comet. SonotaCo shows activity from this direction, but it is not clear that this confirms the existence of this shower (Fig. 12B).

A shower with record high southern declination was added to the Working List under the name e-Velids (#746, EVE). This must be a strong shower on the southern hemisphere, because it was well detected by both CAMS and SonotaCo, despite having a radiant that never rises more than  $10^\circ$  above the CAMS local horizon (Fig. 12C). The shower is caused by a Jupiter-family type comet. It was detected by CAMS in all years when weather permitted observations (2011, 2013 and 2014). The shower belongs to the Puppis-Velid I Complex (#255, PUV). Visual observers from the NAPO-Meteor Section recognized three showers from this area during this timeframe (Jenniskens, 2006, p. 517) which, when drift-corrected to  $\lambda_o = 252^\circ$ , radiate from nearby radiants: the  $\zeta$ -Puppids (#300, ZPU) from  $121.3, -44.3^\circ$  during  $\lambda_o = 219-268^\circ$ , but mostly during  $\lambda_o = 228-237^\circ$  (Jenniskens, 2006, Fig. 29.1); the  $\gamma$ -Puppids (#301, PUP) from  $121.1, -42.3^\circ$  during the period  $\lambda_o = 248-262^\circ$ ; and the b-Puppids (#302, PVE) from  $125.3, -43.9^\circ$  during  $\lambda_o = 249-253^\circ$ , but without a clear peak in activity (Jenniskens, 2006, p. 517). Activity from this area was also noticed in southern hemisphere radar programs (Nilsson, 1964; Gartrell and Elford, 1975). None of the reported positions coincide with the CAMS-detected e-Velids at  $129.5^\circ, -44.2^\circ$  ( $V_g = 44.4$  km/s) during the period  $\lambda_o = 244-257^\circ$ , nor with the new position slightly further south at R.A. =  $130.8^\circ$ , Dec. =  $-46.0^\circ$ , now more data have been added (Fig. 12C). That said, it is possible that the CAMS-detected shower is what was seen as b-Puppids by the visual observers, in which case this shower is now confirmed.

The Northern March  $\gamma$ -Virginids (#749, NMV) were extracted over the period  $\lambda_o = 303-320$ , while an apparent twin shower, the southern March  $\gamma$ -Virginids, were detected later over the period  $337-344^\circ$ . There is evidence, however, that the Northern March  $\gamma$ -Virginids persist to the later period of the southern March  $\gamma$ -Virginids (Fig. 11A). These showers are also detected in SonotaCo data.

Finally, the established  $\alpha$ -Herculids (#346, XHE) were only weakly detected in data up to March 2013 (Jenniskens et al.,

2016a). During the final stages of preparing this manuscript, doubts were raised about the validity of this shower belonging in the IAU List of Established Showers. With additional observations from the cloudy month of March in hand, the shower is now clearly detected both in CAMS and SonotaCo data (Fig. 12D).

#### 4. Properties of the meteor shower population

##### 4.1. Sample selection and nature of identified showers

From the original list of 108 showers reported to the Meteor Data Center in preparation of publication (##643–750), 48 are now dismissed because they could no longer be recognized in the larger 2015 CAMS dataset or in SonotaCo data. Potential showers in the apex source that were no longer detected include: ##646, 648, 649, 654, 661–663, 665, 666, 672–679, 682, 685, 690, 693, 697–700, 702, 704, 721, 722, 735, 737, 740, 741, 743, 744, 747, and 748. Several high-declination showers stand out in the  $II-i$  diagram (inclination versus longitude of perihelion) from which they were originally extracted, but are not clearly detected in the radiant maps. Those include the potential showers ##650, 659, 686, 711, 742, and 745. Antihelion showers that were no longer detected include potential showers ##687, 723, 728, and 730, while the helion source potential shower #725 was now deemed insignificant also. These showers can be removed from the Working List.

That leaves 60 potential showers for study. The 20 newly identified Jupiter-family comet showers with Tisserand parameter  $2.0 < T_J \leq 3.0$  are mostly found in the antihelion source at lower inclinations (Table 1), but some of these slow showers are collected from higher ecliptic latitudes. Searching for clusters in the radiant maps and the  $II-i$  diagram favored streams with unusually low longitude of perihelion  $II$  or relatively high inclination. Usually a small threshold value of  $D_h = 0.05-0.09$  was required to isolate a cluster in the antihelion source itself, but  $D_h = 0.10-0.15$  was used for high declination showers (Table 4). Note that  $D_h$ -criterion searches tended to find some members for almost any starting orbit in these cases.

Three newly identified showers (#680, #710, and #732 in Table 1) have the  $T_J$  significantly larger than 3 expected from an asteroidal source. However, all are sunskirter-comet like showers in inclined eccentric orbits with low perihelion distance.

The 30 newly identified showers with  $T_J \leq 2.0$  that move in retrograde orbits are mostly found in the apex source and caused by long period comets. At times, the apex source has a patchy appearance from multiple showers being active at the same time.  $D$  thresholds in the range  $D_h = 0.15-0.25$  were usually required to isolate the streams.

The 13 newly identified showers with  $T_J \leq 2.0$  in prograde orbits (Table 3) are typically found in the toroidal source and have inclinations in the range  $45-83^\circ$ . Because they are located along a band of activity, showers in the toroidal ring stand out well in our method of shower extraction. The toroidal showers tend to be more diffuse than the apex source showers, but require only a modest  $D_h$ -threshold  $D_h = 0.10-0.16$  for extraction. Some clusters in the  $II-i$  diagram show a range of longitude of perihelion, which cannot be isolated with the single use of a  $D_h$  criterion threshold. Orbital evolution has made the stream members dissimilar in this respect. To extract these streams, we isolated separate parts of the cluster and then combined the sample into one.

##### 4.2. Input to the sporadic background

In total, we assigned 25.6% of all meteors in the March 2013 CAMS database to 230 meteor showers and shower components that could still be detected in the more recent data. Assuming that

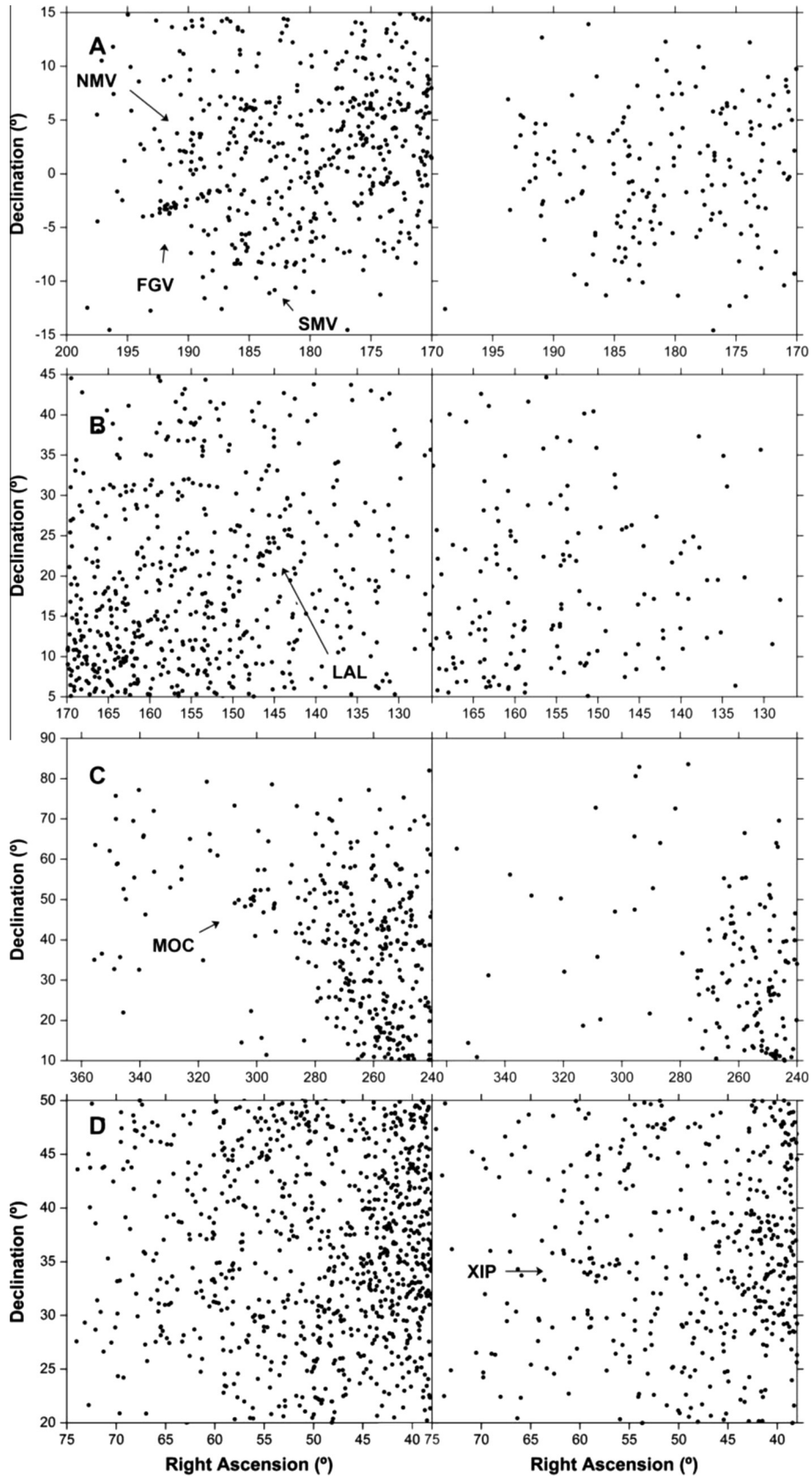


**Fig. 11.** As Fig. 1: (A) the February  $\gamma$ -Virginids (#732, FGV), the Northern March  $\gamma$ -Virginids (#749, NMV) and the Southern March  $\gamma$ -Virginids (#750, SMV) – Period  $\lambda_o = 335$ – $345^\circ$  (drift corrected to  $338^\circ$ ); (B) the  $\lambda$ -Leonids (#733, LAL) – Period  $\lambda_o = 340$ – $344^\circ$ ; (C) the March  $\omicron$ -Cygnids (#734, MOC) – Period  $\lambda_o = 345$ – $349^\circ$ ; (D) the March  $\xi$ -Perseids (#736, XIP) – Period  $\lambda_o = 125$ – $140^\circ$ .

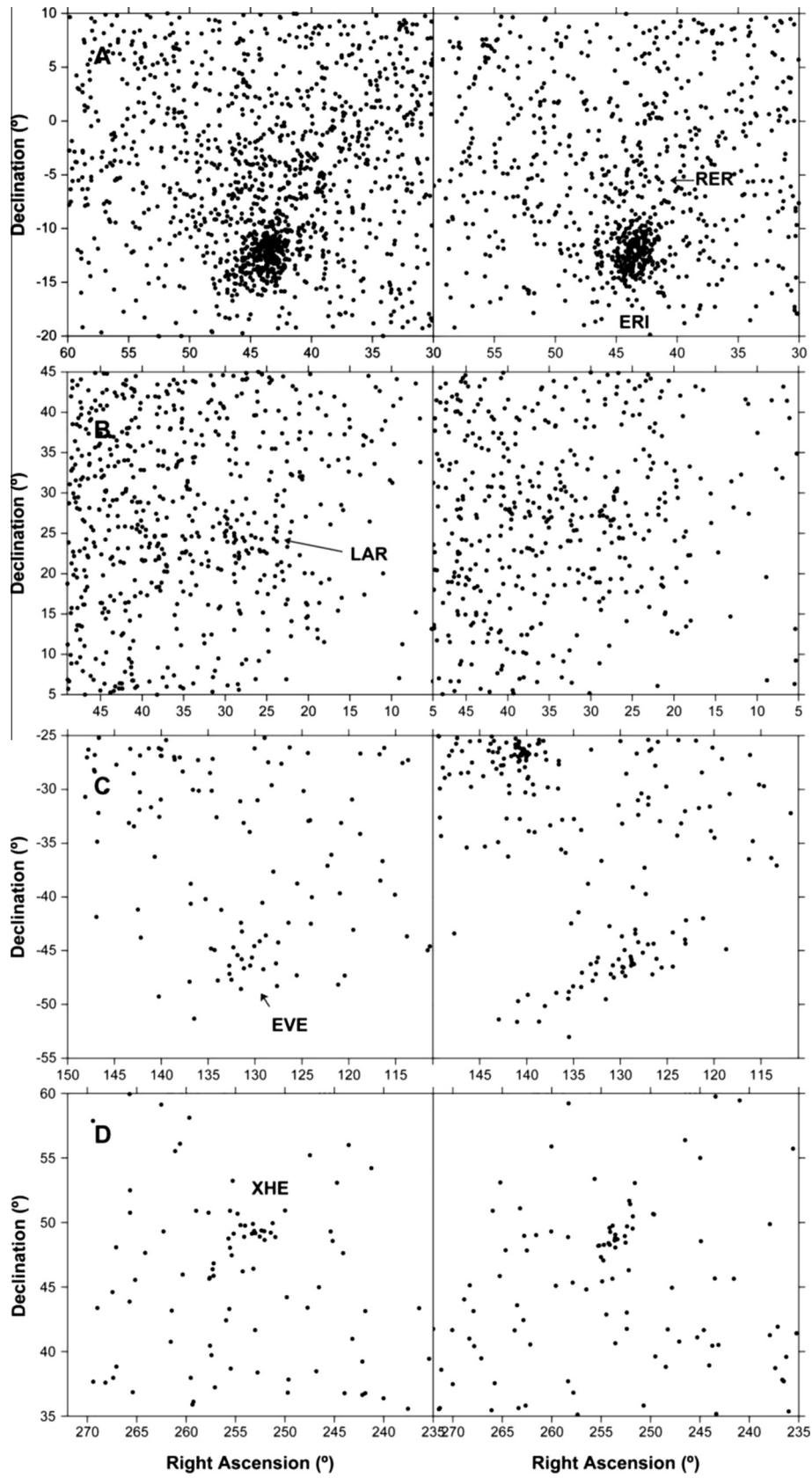


**Fig. 12.** As Fig. 1: (A) the March  $\rho$ -Eridanids (#738, RER) – Period  $\lambda_0 = 127\text{--}149^\circ$ ; (B) the  $\lambda$ -Arietids (#739, LAR) – Period  $\lambda_0 = 150\text{--}157^\circ$ ; (C) the e-Velids (#746, EVE) – Period  $\lambda_0 = 244\text{--}257^\circ$ ; (D) the x-Herculids (#346, XHE) – Period  $\lambda_0 = 348\text{--}353^\circ$ , drift corrected to  $\lambda_0 = 350^\circ$ .

the number of meteors in a given stream ( $N$ ) is a proxy for the strength of the stream, we find that the relative number of streams per bin of  $\log N$  has a power law distribution with exponent  $-0.57 \pm 0.04$ , whereby the log frequency =  $1.94 - 0.57 * \log N$  (Fig. 13).

The sample of extracted showers is complete only down to a membership of about  $N = 10$  meteors per stream. The number of small  $N = 3-7$  showers is not excessive, as would have been the case if many false detections were made. The missing weak showers represent a small percentage of all shower meteors in the database. Extrapolating the power-law fit into the smaller frequency data range down to  $N = 1$  per  $\log N$  bin implies that about 40% of shower meteors are not yet identified as such in the database. If these non-recognized weak showers are included, then we would have assigned 36% of all 110,521 observed meteors to 700 meteor showers.

The strongest showers contribute most significantly to the total count of meteors at the typical CAMS detected visual magnitude of +1. The missing small showers contribute as many meteors as a few of the strongest showers, notably the Geminids and Perseids. This may be related to the fact that the parent body mass distribution, too, is dominated by the larger bodies (Jenniskens, 2006).

Most CAMS-detected meteor showers (132 out of 230) radiate from the apex and toroidal sources with entry speeds of 41–50 (prograde) and 57–72 km/s (retrograde) and have a Tisserand parameter  $T_j \leq 2$ . The meteors are fast and they are caused by relatively small  $\sim 2-3$  mm diameter meteoroids of mass  $\sim 0.001-0.01$  g (Table 5, with masses according to Jacchia et al., 1967).

Most of mass in meteoroid streams, however, arrives on Jupiter-family comet type orbits with entry speeds  $V_\infty = 18-45$  km/s. These slower meteors are caused by 3–7 mm sized meteoroids of mass  $\sim 0.01-0.1$  g (Table 5). Of the observed matter in the form of streams falling onto Earth (a kinetic-energy limited sample), 12% of mass originated from long period and Halley-type comets ( $T_j \leq 2$ ), 71% from Jupiter-family type comets ( $2 < T_j \leq 3$ ), 2% from asteroidal sources other than the Geminids ( $3 < T_j$ ), and 15% from the asteroidal Geminids alone ( $T_j \sim 4.4$ ).

These fractions may not fully reflect the input of meteoroids to the interplanetary dust cloud. The Geminids are a transient shower, expected to fade by AD 2200 (Jenniskens, 2006), and may not contribute in the same way to the interplanetary dust cloud as a whole. Also, the Jupiter-family type showers disperse

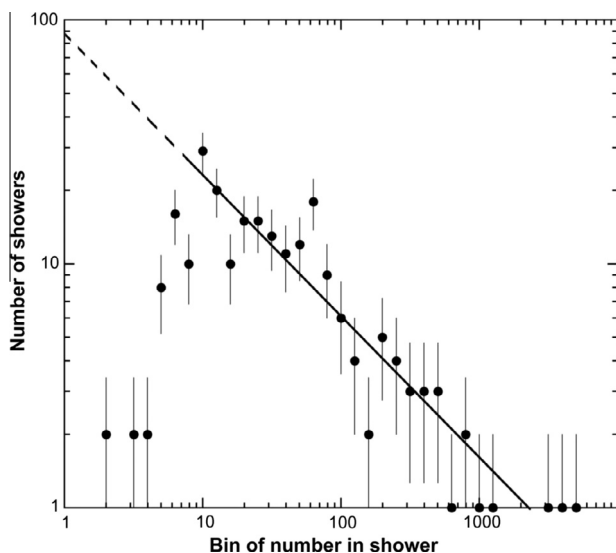


Fig. 13. The size-frequency distribution of all identified meteor showers with a count of  $N$  members among the  $\sim 110,000$  CAMS meteoroid orbits.

Table 5

Detection limits – the typical size (in mm) of CAMS-detected meteoroids at the median value of the magnitude distribution, and the characteristic threshold of meteoroid diameters above which all meteors are detected.

$V_\infty$ (km/s)	CAMS <sup>a</sup> median	CAMS <sup>a</sup> threshold	CMOR threshold	AMOR threshold
11.2	10.6	34.4	1.53	0.21
13	9.7	28.6	1.29	0.18
15	8.4	24.8	1.08	0.15
18	7.1	20.2	0.87	0.12
20	6.4	18.1	0.81	0.11
30	4.0	11.6	0.47	0.066
40	3.0	8.4	0.33	0.046
50	2.5	6.8	0.25	0.036
60	2.1	5.6	0.20	0.029
72	1.8	4.8	0.16	0.023

<sup>a</sup> Mass calculated according to Jacchia et al. (1967), taking into account the different definition of the magnitude scales  $m_v = m_{ph} + 0.6$  and assuming a particle density of  $\rho = 1$  g/cm<sup>3</sup>. The diameter is a factor of 1.6 larger if  $\rho = 0.25$  g/cm<sup>3</sup>, instead.

more rapidly by planetary perturbations and are sooner lost in the sporadic background than many other types. Even asteroidal streams are expected to disperse more slowly. We did not assign meteors to meteor showers if their distribution was too much dispersed to make it stand out from the sporadic background. Indeed, Jupiter-family type showers identified so far tend to have relatively high  $>20^\circ$  inclinations, with radiants at high ecliptic latitude where the sporadic background is weak. Hence, it is conceivable that the remaining population of meteoroids in JFC-like orbits contains a relatively high fraction of unrecognized streams with inclinations  $<20^\circ$ . That could increase the total number of showers above 700 and the percentage of meteors assigned to showers above 36%. Alternatively, this material can be thought of as a relatively young component to the sporadic population.

### 5. Properties of the sporadic background

Fig. 14 shows the CAMS detected sporadic background that remains after removing all known and newly identified showers and shower components as identified in the CAMS database up to March of 2013, not including those showers that were later dismissed (Jenniskens et al., 2016a, 2016b; Jenniskens and Nénon, 2016; and this work). Table 5 defines the median particle size of the detected meteoroids as a function of entry speed  $V_\infty$ .

Because we carefully examined each meteoroid orbit during data reduction, this background is expected to be relatively devoid of false detections ( $<2\%$ , Jenniskens et al., 2011). Some residual shower signal can still be recognized, despite carefully isolating the showers from the sporadic background. The top left diagram of Fig. 14 shows a ghostly image of the “Orionid tail” of showers (Jenniskens et al., 2016a), for example.

#### 5.1. As-observed orbital element distributions

Individual panels in Fig. 14 show the as-observed radiant distribution of several sporadic meteor populations defined by a range in Tisserand parameter. Fig. 15 shows the corresponding orbital element distributions. Pertinent properties are summarized in Table 6.

The radiant distribution of the Encke-like and asteroid-like groups are surprisingly similar to that of the Jupiter-family comet dust. A similarly shaped antihelion source is recognized in the distribution of the  $2.0 < T_j \leq 3.0$  typical of Jupiter-family comet orbits (Fig. 14, upper right panel), the  $3.0 < T_j \leq 3.2$  typical of the Taurids

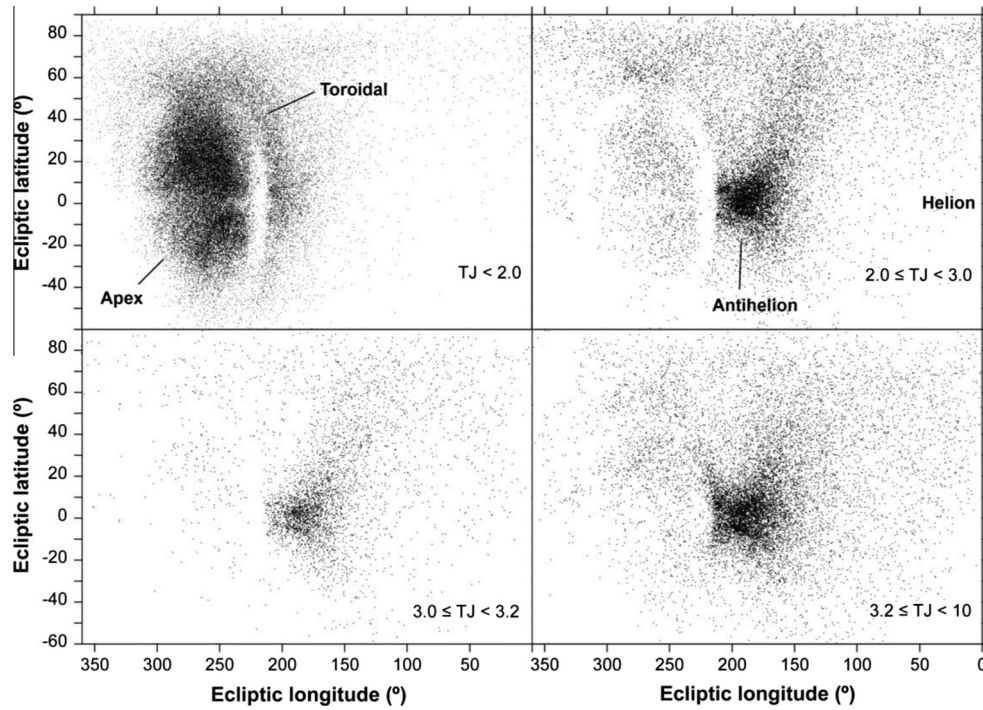


Fig. 14. The sporadic background of meteors observed by CAMS (median value: +1.2 magn.), after removal of the identified meteoroid streams. Data are separated in four intervals of Tisserand parameter  $T_J$ . Sporadic sources are identified.

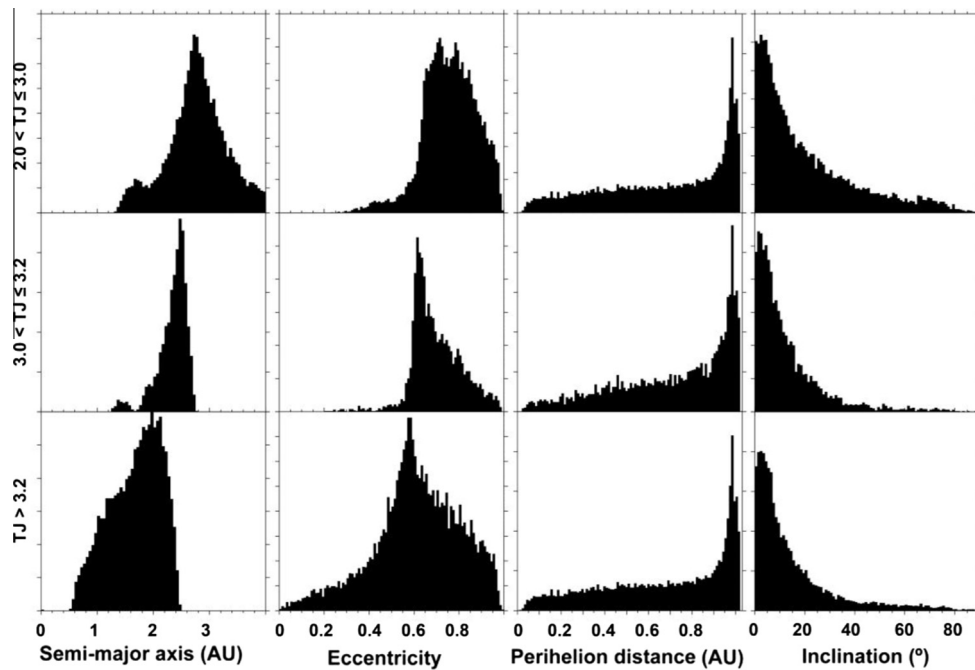


Fig. 15. Orbital element distributions for all as-observed CAMS-detected sporadic meteors with (from top to bottom)  $2.0 < T_J \leq 3.0$ ,  $3.0 < T_J \leq 3.2$ , and  $T_J > 3.2$ , respectively.

from Comet 2P/Encke (Fig. 14, lower left panel), and the  $T_J > 3.2$  on near-Earth asteroid-like orbits (lower right panel). The  $T_J > 3.2$  component has more low- $q$  orbits responsible for an additional arc of radiants in the toroidal ring, and less  $i \sim 0^\circ$  orbits with radiants near the ecliptic plane.

There is no excess of  $q \sim 0.33$  AU orbits for the  $3.0 < T_J \leq 3.2$  population, so the Taurid showers are not the only source of this sporadic population (Fig. 15). The orbital element distribution is

surprisingly similar to that of JFC-like meteoroids, except with eccentricities and semi-major axis at the lower range.

Again, the majority of CAMS-detected meteors (60%) arrive on orbits with  $T_J \leq 2.0$  from Halley-type and long period comets (HTC/LPC). The population with  $T_J \leq 0.0$  isolates the apex source of mostly retrograde orbits, while  $0.0 < T_J \leq 2.0$  combines the toroidal source with the remainder of the apex source (not shown in Fig. 14, but separately tabulated in Table 6).

**Table 6**  
Parameters of CAMS-detected sporadic meteor populations.

Component	LPC	HTC or LPC + P-Rdrag	JFC	Encke or JFC + P-Rdrag	Asteroid or JFC + P-Rdrag
Tisserand parameter – $T_J$	$\leq 0.0$	0.0–2.0	2.0–3.0	3.0–3.2	$> 3.2$
Source	Apex	Apex/Toroidal	Antihelion	Antihelion	Antihelion/toroidal
Number detected (%)	27	33	18	5	17
Threshold mass (g)	0.07	0.13	0.83	1.02	1.62
Diameter (mm)	5.1	6.3	11.7	12.5	14.6
Mass dist. index – $s$	$2.32 \pm 0.04$	$2.20 \pm 0.05$	$2.29 \pm 0.03$	$2.35 \pm 0.06$	$2.60 \pm 0.12$
Magn. dist. index – $\chi$	$3.39 \pm 0.11$	$3.03 \pm 0.13$	$3.29 \pm 0.09$	$3.48 \pm 0.18$	$4.38 \pm 0.47$
Observing efficiency	0.892	1.000	0.899	0.968	0.965
Number of $\geq 0.028 \text{ g}^a$ (%)	1	1	13	7	78
Total mass $\geq 0.028 \text{ g}^a$ (%)	1	2	17	9	71
Total mass $\geq 1 \text{ g}^a$ (%)	1	5	31	13	50
Median $V_\infty$ (km/s)	67.6	57.0	28.1	22.4	22.7
Peak of $a$ (AU)	7.2	3.73	2.73	2.48	2.05
Peak of $e$	0.97	0.97	0.77	0.62	0.58
Peak of $i$ ( $^\circ$ )	155	$69 + 137$	0	2	3
Number ratio $k_c - A/C$	0.21	0.32	0.52	0.81	1.36

<sup>a</sup> Corrected for observing biases.

Again, the slow antihelion source meteors dominate the mass influx because the CAMS-detected meteors are a kinetic energy (and luminous efficiency) limited sample, of which fast meteoroids are more efficiently detected than slow meteoroids of the same mass (Table 5). Masses for each meteoroid were calculated using Jacchia et al. (1967), which assumes a mass  $M \sim V_\infty^{-3.89}$ .

The mass distribution of each Tisserand parameter group is a power law distribution down to a threshold mass, above which all meteors are detected (Table 5). The slope of this distribution defines the differential mass distribution index ( $s$ ):  $\Delta N(M) \sim M^{-s} \Delta M$ . From this, the magnitude distribution index  $\Delta N(m) \sim \chi^m \Delta m$  follows from  $s = 1 + 2.5 \log(\chi)$ .

Results for  $s$  and  $\chi$  are tabulated in Table 6. The CAMS-detected  $T_J \leq 3.2$  sporadic meteor populations have an observed mass and magnitude distribution similar to that measured previously from visual and video observations ( $\chi = 3.4$ ). The  $T_J > 3.2$  group, however, has a distribution equal to the  $\chi = 4.3$  measured by radar for +8 to +10 magnitude meteors (Jenniskens, 2006; Campbell-Brown, 2008).

All slopes have  $s > 2.0$  ( $\chi > 2.5$ ), so that most sporadic mass is in the smaller particles for all sources. This is contrary to most meteor showers, which are typically dominated by the larger meteoroids or have equal mass per mass interval (Jenniskens, 2006).

After including the under-sampled small-mass range of the distribution to a threshold mass for each component, and after correcting for how efficient each component is observed according to factors listed in Table 6 (see Section 5.2), the corresponding mass fractions are listed in Table 6 for two different mass thresholds of 0.028 g and 1.0 g. Unlike meteor showers, for which we know very few that have  $T_J > 3.2$  (Section 4.2), as much as 71% of mass falling in from the as-observed sporadic meteor population with masses  $M > 0.028 \text{ g}$  arrives on  $T_J > 3.2$  asteroid-like orbits.

Assuming that the unobserved helion source is as strong as the antihelion source, both caused by the same meteoroid population, then this population (counting all orbits with  $T_J > 2$ ) is responsible for 98% of the mass influx to Earth in the 0.028–30 g range and about 97% in the 1–30 g range (Table 6).

## 5.2. Observing bias corrected and mass weighted distributions

Previous studies have defined the antihelion source differently, by selecting a range of ecliptic latitude and longitude of the radiant (Taylor and Elford, 1998; Galligan and Baggaley, 2005; Campbell-Brown, 2008). Fig. 16 compares the CAMS-derived orbital element distributions for the antihelion source restricted

now to sun-centered radiants with ecliptic longitude  $110^\circ < \lambda < 210^\circ$  and latitude  $-30^\circ < \beta < +30^\circ$ , chosen to match the range adopted by Galligan and Baggaley (2005) when analyzing AMOR data. Note that Campbell-Brown (2008) defined the antihelion source narrower as  $177^\circ < \lambda < 217^\circ$  and  $-11^\circ < \beta < +11^\circ$  for the CMOR data.

The orbital element distributions in Fig. 16 were corrected for in-atmosphere observing bias effects and mass weighted, but not corrected for collision probability with Earth. The in-atmosphere observing biases that affect the radar detection efficiency include the atmospheric properties and attenuation from initial train radius, finite velocity factor, pulse repetition rate factor, and Faraday rotation reduction factor (Galligan and Baggaley, 2004). The detection efficiency varies for meteors with radiants at different positions in the sky and by how deep they penetrate into the atmosphere. The detection efficiency is also a combination of their mass and speed, and affected by fragmentation. At each entry speed, there is a threshold mass above which the detection efficiency no longer depends on meteor mass (Table 5).

The following in-atmosphere observing biases apply to the CAMS optical observations, which were applied by giving each meteor a weight factor inversely proportional to the likelihood of it having been detected. The detection efficiency depends on the effective collecting area, depending on how long a given radiant is above the horizon. For the CAMS latitude  $\varphi = +37^\circ \text{N}$ , a given apparent declination in the range  $\varphi - 90^\circ < \delta < 90^\circ - \varphi$ , the radiant will be above the horizon for a time proportional to  $\cos^{-1}((-\sin \varphi \sin \delta) / (\cos \varphi \cos \delta)) / 180^\circ$ . Over time, all right ascensions are sampled.

Geometric dilution lowers the flux of meteoroids approaching from near the horizon, with the observed flux proportional to about  $\sim \sin(h_r)$ , with  $h_r$  the radiant elevation.

Over time, not all ecliptic longitudes are sampled in the same way, with values near the Sun unobserved by daytime if  $\varphi - 90^\circ < \delta < 90^\circ - \varphi$ . Based on the observed distribution of meteor apparent radiants, we only consider radiants with sun-centered ecliptic coordinates  $(\lambda, \beta)$  with  $90^\circ < \lambda < 270^\circ$  more than  $\cos^{-1}(\cos \lambda \cos \beta) > 50^\circ$  from the position of the Sun, which removes any meteors detected from the helion source.

Also, because slower meteors are detected deeper into the atmosphere, the effective surface area varies with entry speed. Based on the observed meteors, the standard deviation of the latitude ( $\phi$ ) of the beginning height varies with speed as:  $\sigma_\phi (^\circ) = 0.53 + 0.002V_\infty - 760V_\infty^{-3.5}$ , with  $V_\infty$  in km/s.

To arrive at a distribution of meteoroids at a constant limiting mass, each meteor is weight inversely proportional to what fraction of meteors is detected down to that mass. Based on the

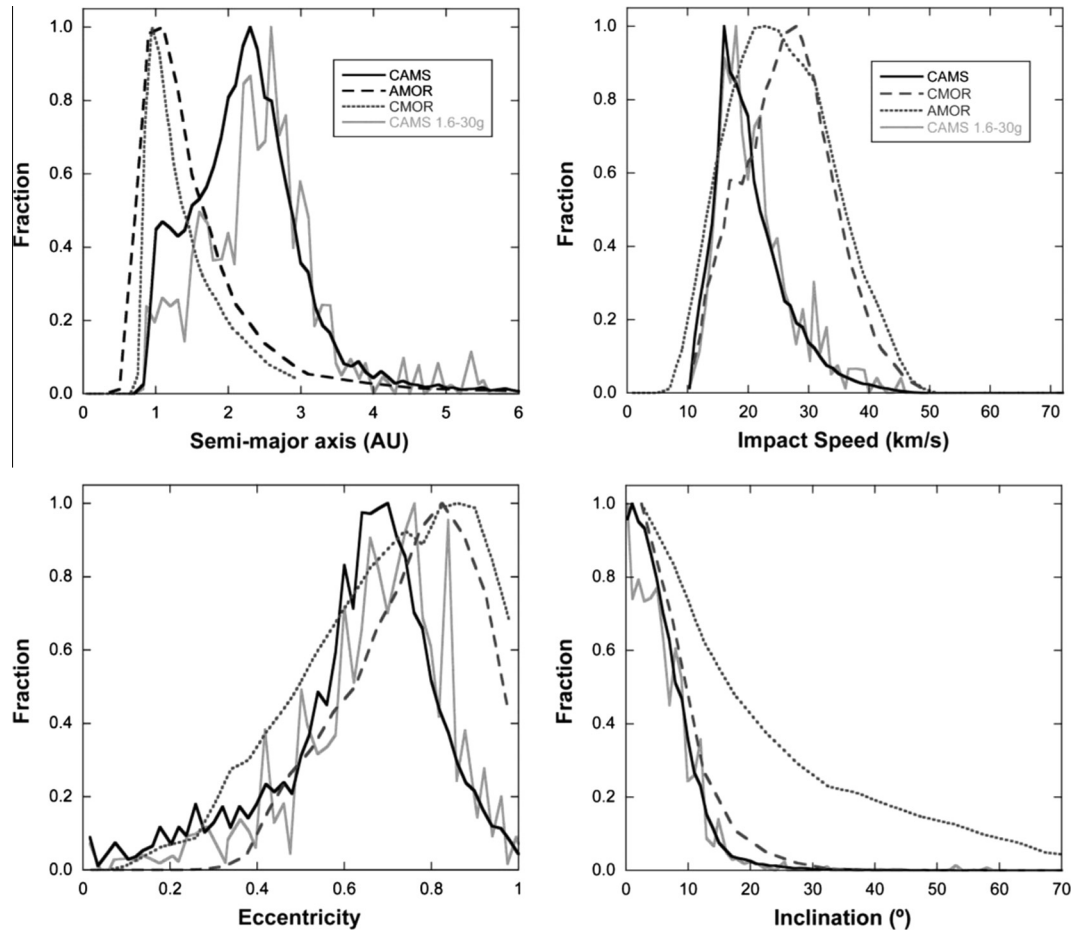


**Fig. 16.** The normalized distribution of observed entry speed and orbital elements from directions that define the antihelion source more narrowly as having sun-centered radiant with ecliptic longitude  $110^\circ < \lambda < 210^\circ$  and latitude  $-30^\circ < \beta < +30^\circ$ . CMOR data (dashed line) are after Campbell-Brown (2008), while AMOR data (dotted line) are after Galligan and Baggaley (2005). Data are corrected for in-atmosphere observing biases and mass-weighted, but not corrected for Earth-collision probability. CAMS results in a thick gray line are for a threshold mass of 1.6 g, above which the sample is complete, while the thin solid line shows all data with mass weighing according to  $\sim V_\infty^4$ .

Jacchia et al. (1967) mass distribution as a function of velocity, the typical size of detected meteors is listed in Table 5. The median values are best matched by  $\log(M) = 3.0 - 3.0 \log(V_\infty)$ , suggesting a  $V_\infty^{-3.0}$  dependence, slightly weaker than in the Jacchia et al. equation. The threshold mass, above which the distributions suggest all meteors are detected is proportional to  $\sim V_\infty^{-3.1}$  (Table 5). The log number of meteors is proportional to  $(s-1)\log M$ . Values of  $s$  are listed in Table 6. Together, the rate of observed meteors increases with speed according to  $V_\infty^{4.0}$ .

Alternative to mass-weighting the sample, we imposed a mass cut-off at 1.6 g, high enough for the detection efficiency to be no longer velocity-dependent. This limits the total sample to only 498 meteors with masses up to about 30 g. Results are shown as a thick gray line in Fig. 16. The distributions are more noisy, but generally in good agreement to the all-data mass-weighted distributions.

This comparison brings out how the larger CAMS-detected meteoroids have a distinctly different semi-major axis distribution than those detected by CMOR and AMOR. Instead of peaking at  $a = 0.8\text{--}1.5$  AU like CMOR and AMOR, the CAMS distribution peaks at  $a = 2.1\text{--}2.8$  AU (Fig. 16). The mass-influx dominant  $T_J > 3.2$  group contains most of the  $a < 2$  AU meteoroids and those with low eccentricities.

### 5.3. Distribution of meteor beginning heights

The mass-influx dominant  $T_J > 3.2$  group does also manifest in the distribution of meteor beginning heights ( $H_b$ ) as a function of

entry speed (Fig. 17). The distribution appears to show distinct high, low and intermediate values (Ceplecha, 1967, 1988). It is striking how particles with  $V_\infty < 13$  km/s have only relatively low beginning heights (Weryk et al., 2013). These slow meteors belong mostly to the  $T_J > 3.2$  group.

It is possible to quantify this difference. The meteor's beginning height is thought to reflect the moment the particle heats up sufficiently to start thermal ablation of its minerals (Whipple, 1954). Based on a simple one-dimensional solution of the heat-conductivity problem during the initial part of the meteor trajectory, Whipple (1954) derived an equation that gives the particle surface temperature as a function of altitude (expressed as air density). He formulated a “k-criterion” that describes how much different the particle behaves under the same expected entry speed, air-density, and radiant altitude dependencies. Ceplecha’s (1967, 1988) modified formalism ( $k_b$ ) assumes that the particle surface temperature changes with  $V_\infty^{2.5}$ , but CAMS-detected meteors show a more gradual change of beginning height, expected from a surface temperature dependency according to  $V_\infty^{2.0}$ . Along lines pursued by Abe et al. (2014), we can formulate a  $k_c$  criterion:

$$H_b \text{ (km)} = k_c - (2.86 - 2.00 \log V_\infty \text{ (km/s)})/0.0612 \quad (1)$$

written in this way because we take the air density approximately as:  $\log \rho \text{ (g/cm}^3\text{)} = -2.86 - 0.0612 H_b \text{ (km)}$  for the 120–40 km range of  $H_b$  (Öpik, 1958). This equation fits the general behavior of the beginning heights for an adopted value of  $k_c$  in the range

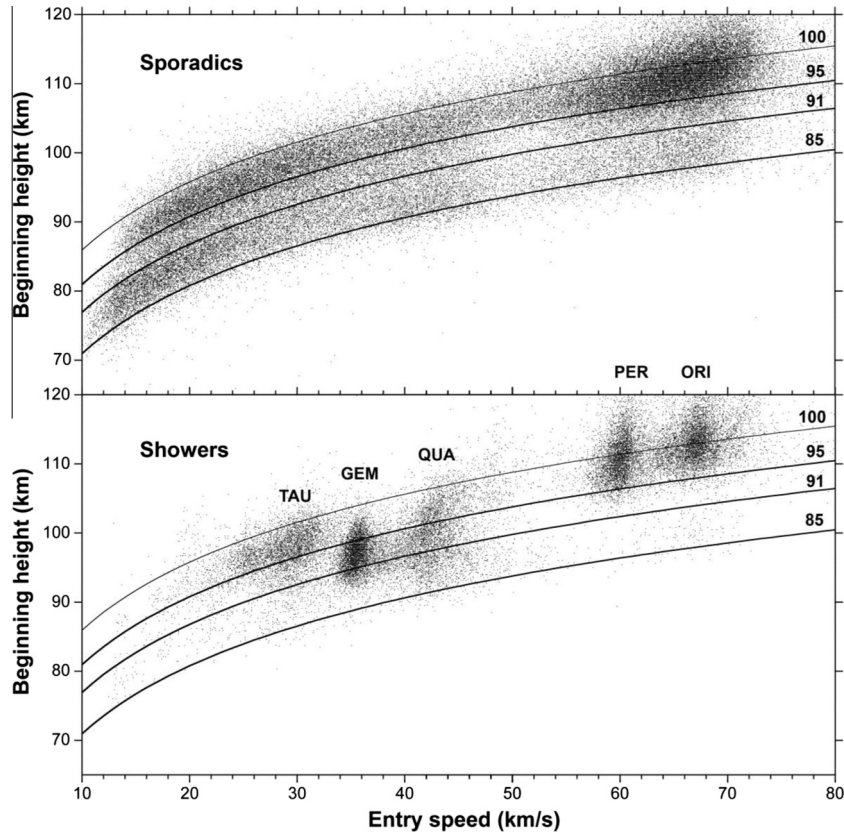


**Fig. 17.** The beginning height of CAMS-detected sporadic (top) and shower (bottom) meteors as a function of entry speed ( $V_\infty$ ). Lines depict constant surface temperature for particles with different  $k_c = 85\text{--}100$  km.

85–100 km (Fig. 17). According to Eq. (1) of Ceplecha (1967), after forcing a  $V_\infty^2$  dependence:

$$k_c = (-1/0.0612) * \log((2T/A) * \sqrt{[\lambda\rho_m C_p b \cos(z_r)]}) \quad (2)$$

$T$  is the surface temperature where the meteor first becomes detectable,  $\lambda$  the heat conductivity,  $C_p$  the specific heat capacity of the material,  $A$  the heat transfer coefficient,  $\rho_m$  the meteoroid density,  $z_r$  the zenith distance of the radiant, and  $b$  the air-density gradient. The latter two parameters have little impact on the result, so that most differences in  $k_c$  are expected to be a consequence of the thermal properties of the meteoroid.

From Fig. 17, the CAMS-detected population with low-beginning heights has  $k_c = 85\text{--}91$  km (Ceplecha’s group A), while the higher group typical of the Taurids, Perseids and Orionids has  $k_c = 95\text{--}100$  km (Ceplecha’s groups C1–C3). The intermediate group typical of the Geminid and Quadrantid/Southern  $\delta$ -Aquiriid showers (Fig. 17) has  $k_c = 91\text{--}95$  km (Ceplecha’s group B). Note that both the asteroidal Geminids ( $T_j \sim 4.4$ ) and the Quadrantids and Southern  $\delta$ -Aquiriids of the Comet 96P/Machholz complex, experienced some level of heating from past or present  $q < 0.1$  AU orbits (Jenniskens et al., 2016a).

All Tisserand parameter groups contain meteors that span the full range of  $k_c$ . However, the ratio of low  $k_c < 91$  km (group I) to high  $k_c > 95$  km (group III) increases with increasing  $T_j$ . The  $T_j > 3.2$  component dominates the low  $k_c$  group at speeds  $V_\infty < 25$  km/s.

#### 5.4. Implications for dynamical models of interplanetary dust

Over time, planetary perturbations will cause all meteoroid streams to disperse into a sporadic background, which will evolve under Poynting–Robertson (P–R) drag and fade when meteoroids collide or disrupt by other processes (Jenniskens, 2006; Williams,

2011). The Poynting–Robertson drag is due to absorbed light being re-emitted with a small Doppler shift in wavelength relative to the motion of the meteoroid (Poynting, 1903; Roberston, 1937), and lowers the semi-major axis and eccentricity of prograde eccentric orbits over time (Wyatt and Whipple, 1950). The collisional lifetime is often taken from Grün et al. (1985), who assumed that meteoroids disappear from the population in catastrophic collisions with other (mostly smaller) meteoroids, being destroyed more rapidly when the particles are larger.

An important result from our observations is that among mm–cm sized particles is a population of P–R evolved particles with low semi-major axis and eccentricity (Figs. 15 and 16). They also have different thermal properties on average, as expressed by  $k_c$  (Fig. 17). For P–R drag to change the semi-major axis of an eccentric  $e \sim 0.7$  spherical particle with density  $1 \text{ g/cm}^3$  from  $a = 2.3$  AU to  $1.0$  AU takes about  $3 \times 10^6$  years for a 7-mm particle (CAMS),  $3 \times 10^5$  y for a 0.6-mm particle (CMOR), but only  $4 \times 10^4$  y for an 0.09-mm particle (AMOR), during which the eccentricity evolves to  $e \sim 0.44$  in all cases (Wyatt and Whipple, 1950).

These ages are much longer than the respective collisional lifetimes estimated by Grün et al. (1985). Grün et al. calculated that at 1 AU heliocentric distance,  $d = 7$  mm particles had a collisional lifetime of only  $\tau_{col} = 8,000$  y, while 0.6-mm lasted 16,000 y, and 0.09-mm 250,000 y, respectively.

Meteoroids are more abundant at shorter radial distances from the Sun. As a result, the collisional timescales are much shorter at 0.1 AU. According to Grün et al.:  $\tau_{col} = 20$  y, 200 y and 3,200 y, respectively. On eccentric orbits, the particles spend most time near aphelion, at  $Q \sim 4.1$  AU for CAMS meteoroids and  $Q \sim 1.8$  AU for CMOR and AMOR meteoroids, but are preferentially destroyed near perihelion. This increases the collisional lifetimes by about a factor of 10 depending on the perihelion distance. The relevant

collisional timescales are  $\tau_{col} \sim 100,000$  y,  $\sim 30,000$  y and  $\sim 400,000$  y for typical CAMS, CMOR and AMOR detected meteoroids, respectively.

Nesvorný et al. (2011) pointed out that the time needed to evolve CMOR-detected meteoroids by P–R drag was a factor of 4–10 larger than the Grün-model collisional lifetime. The Nesvorný et al. (2010) model was modified by adopting a  $\tau_{col} = 1\text{--}3 \times 10^5$  y collisional lifetime for CMOR particles (testing values of 0.3, 1, 3, 10,  $\dots \times 10^5$  y), a value similar to that assumed for AMOR particles. They also accelerated the evolution by assuming that the disruption of JFC's in the inner Solar System is proportional to  $q^{0.75 \pm 0.25}$  (Di Sisto et al., 2009). This puts more particles initially on faster evolving short  $q \sim 0.5$  AU orbits, rather than the  $q \sim 2.5$  AU preferred from a slowly evolving ice sublimating JFC population.

The same can now be said for the CAMS-detected meteoroids with  $T_J > 3.2$ . These  $\sim 7$ -mm grains survive collisions for  $\tau_{col} \sim 1.1 \times 10^6$  y to evolve from  $a = 2.75$  to  $a = 2.02$  AU and lower the eccentricity peak from  $e = 0.63$  to  $e = 0.58$  of the high  $T_J$  population, and about  $\sim 3 \times 10^6$  y to evolve from  $a = 2.3$  AU to 1.0 AU. According to Grün et al. (1985), they should exist no longer than  $\sim 1 \times 10^5$  y. The implication is that while the Grün et al. model assumes that larger meteoroids are more prone to collisions than smaller meteoroids, it appears the opposite is true.

It is not clear why the CMOR and AMOR populations have the observed high eccentricities. The CAMS-detected  $T_J > 3.2$  population is likely the same population as seen by the CMOR at the high-mass slope of the mass influx curve and by the AMOR at its peak (Nesvorný et al., 2011). However, P–R drag is expected to lower the eccentricity over time, rather than increase it. The eccentric orbits detected by CMOR and AMOR result in a higher impact speed (Fig. 16). It is possible that the slow entry speed component of the sporadic influx is not observed, if the radar detection efficiency for slow meteors is overestimated.

Given the long evolution timescale of the P–R evolved population, it is surprising how strong is the component of dust with  $a \sim 2.1\text{--}2.8$  AU still in JFC-like orbits among CAMS-detected meteoroids (Fig. 16). For masses  $\geq 0.028$  g, the JFC- and Encke-like populations represents 26% of mass influx, the  $T_J > 3.2$  population accounts for 71% (Table 6). If collisions do not efficiently remove grains, then the JFC population ought to be  $\sim 3 \times 10^5$  y old. However, during such a long time, the population should have evolved to  $T_J > 3.2$ .

Instead, we suggested that perhaps the larger CAMS-detected grains in JFC-like orbits are physically weak and disrupt in a few thousand years by non-collisional processes that weaken the Van der Waals or other binding forces that keep the grains together. This could be due to thermal stresses, centrifugal forces from spin-up, charge repulsion, or loss of volatile organic glue in the particles, amongst others. When they disrupt, the larger particles would produce a population of mm-sized and smaller grains. These and the remaining large grains could be more resistant to such effects (Nesvorný et al., 2011).

Such a disruption of the grains would account for the short lifetimes required for larger masses in the Grün et al. (1985) model to explain the observed mass influx at Earth, except that collisions are not what limits their lifetime.

Evidence for meteoroid disruption also comes from the dynamical evolution of meteoroid streams. A lack of true twin showers among the Taurids, for example, implies that the Taurid shower meteoroids do not survive the interplanetary medium long enough ( $\leq 10^4$  y) to fully rotate the nodal line in differential precession (Jenniskens et al., 2016a). With  $q \sim 0.33$  AU, the collisional lifetime according to Grün et al. (1985) is only  $\tau_{col} \sim 10^4$  y. On the other hand, if the collisional lifetimes are much longer as implied by the presence of a P–R evolved population among mm–cm sized

grains, processes other than collisions must remove meteoroids from these streams.

The strength of the young JFC-like component in CAMS data reflects the balance between dust production from the disruption of Jupiter-family comets Jenniskens (2008a,b) and the loss of meteoroids by meteoroid disruption. From the mass influx curve (Jenniskens, 2006, Fig. 32.1), the relative mass in the evolved and the young populations summed over the full meteoroid mass range  $\leq 1$  kg is about  $f = 200$  if the young population dominates at 1 kg and initially has a rising distribution with mass index  $s = 1.75$ . Assuming mass is conserved, this implies for the dominant larger meteoroids in the JFC-like component that the disruption timescale is of order  $\tau_d = 3 \times 10^5 / f = 300$  y, where  $3 \times 10^5$  is taken to be the age of the AMOR and CAMS meteoroids at the peak of the mass influx curve. For the sporadic component detected here ( $s = 2.32$ ) with a relative mass at 0.2 g of about 1/3 of that of the evolved component, this fraction is  $f \sim 30$ . Indeed, for the magnitude distribution to steepen over time from  $s \sim 1.75$  during ejection, to  $s \sim 2.00$  in annual streams and  $s = 2.32$  in the sporadic background, the disruption lifetime has to increase from  $\tau_d \sim 300$  y for  $\sim 1$  kg masses to  $\tau_d \sim 10^4$  y for the smaller  $\sim 0.2$  g masses. The high-mass slope of the mass-influx curve steepens over time when larger particles continue to disrupt until a balance is reached between input and removal.

That leaves the question what is responsible for the shape of the low-mass slope of the mass influx curve. At these small 0.01–0.1 mm sizes, the evolution is determined by the rate of loss due to P–R drag or by collisions. If P–R drag dominates, the eccentricity distribution at Earth should evolve rapidly toward  $e = 0.05$  (Nesvorný et al., 2011), while if collisional lifetimes are short enough ( $\tau_{col} \sim 2 \times 10^4$  y at 0.1 mm and  $\tau_{col} \sim 10^3$  y at 0.01 mm) then eccentricities will evolve to an intermediate value. Fraunhofer line observations of the zodiacal cloud suggest that  $e = 0.3\text{--}0.5$  for 10–100  $\mu\text{m}$  grains (Ipatov et al., 2008). AMOR, too, shows a population of particles with such intermediate eccentricities (Fig. 16). This suggests that our current zodiacal cloud models can be improved by decreasing the collisional lifetime in this size regime. For the population observed at Earth as a whole,  $\tau_{col} \sim 6 \times 10^5 * d^{1.4}$  year, with  $d$  the grain diameter in mm.

## 6. Conclusions

We searched the March 2013 CAMS database of  $\sim 110,000$  meteoroid orbits visually for clusters in sun-centered radiant coordinates and  $II-i$  orbital element space using the  $D_h$ -criteria only to extract the cluster from the background. 26% of meteors were assigned to 230 meteor showers and shower components. 70 are already in the IAU List of Established Meteor Showers, after 26 were confirmed by CAMS. An additional 55 previously known showers in need of confirmation were validated, for a total of 81 verified showers. 19 new shower components were identified that are in need of validation. 86 new showers were discovered, 54 of which are also present in the SonotaCo meteoroid orbit database (30 of which are discussed in this paper). The other 32 newly detected showers presented here are still in need of validation.

From the size frequency distribution of detected showers, we deduce that 36% of all meteors belong to showers above the  $N = 1$  per 110,000 shower limit. Most showers were detected in the apex and toroidal sources, but these are fast meteors, each of which is caused by a small meteoroid. 71% of mass that enters Earth's atmosphere from CAMS-detected showers arrives at Earth on Jupiter-family comet orbits. That fraction may well be underestimated, because Jupiter-family comet showers can be dispersed rapidly by gravitational forces, forming a relatively young sporadic background component.

After removing all identified showers, the remaining CAMS-detected sporadic background has semi-major axis  $a \sim 2.1$ – $2.8$  AU, close to that of its source (mostly dormant and weakly active Jupiter-family comets). This is in contrast to distributions measured by CMOR and AMOR, which have  $a \sim 0.8$ – $1.5$  AU. The mass-dominant  $T_j > 3.2$  component is evolved by Poynting–Robertson drag. This requires a collisional lifetime  $\sim 1$ – $3 \times 10^6$  y, a factor  $\sim 10$  larger than calculated in the Grün et al. (1985) model.

Only a small fraction of large particles survive to evolve this much. As much as 26% of mass in the  $\sim 7$ -mm size range falls into Earth on JFC-like orbits, much of the remainder from the P–R evolved component. Such a large contribution implies that these meteoroids are lost in about  $10^4$  y, possibly from disintegrating into smaller grains by processes other than collisions. This can leave a fraction of large grains to evolve by P–R drag that are more resilient to the mechanisms at work. Those remaining grains appear to have somewhat different thermal properties, because the onset of ablation is delayed during atmospheric entry.

More reliable age estimates for the antihelion source sporadic components will follow from a modeling effort of the de-biased meteoroid populations, which is outside the scope of this paper. The meteoroid orbit surveys are ongoing and future work is aimed at confirming the newly detected showers. All confirmed showers are suitable anchor points for dynamical meteoroid stream models, if potential parent bodies can be identified.

## Acknowledgments

We thank all CAMS team members for their support of the project: amateur astronomers and students who helped build CAMS, supporting CAMS operations over the years, and assisted in the ongoing data reduction effort. We also thank David Nesvorný for helpful discussions during the preparation of this manuscript. Fremont Peak State Park and Lick Observatory generously hosted the deployment of the CAMS camera stations. The CAMS project was made possible by grants from NASA's Planetary Astronomy (NNX08AO64G) and Near Earth Object Observation (NNX12AM14G) programs.

## References

- Abe, S. et al., 2014. Orbital evolution of Geminids and Quadrantids by middle and upper atmosphere radar observations. In: Muinonen, K. et al. (Eds.), *Asteroids, Comets, Meteors 2014*. Proceedings of the Conference Held on 4 July 2014 in Helsinki, Finland, 1pp (abstract).
- Andreic, Z. et al., 2014. Results of CMN 2013 search for new showers across CMN and SonotaCo databases I. *J. Int. Meteor. Org.* 42, 90–97.
- Bettonvil, F., Johannink, C., Breukers, M., 2014. CAMS BeNeLux. In: Rault, J.-L., Roggemans, P. (Eds.), *Proceedings of the International Meteor Conference, Giron, France, 18–21 September 2014*. International Meteor Organization, pp. 55–58.
- Brown, P. et al., 2010. A meteoroid stream survey using the Canadian Meteor Orbit Radar – II: Identification of minor showers using a 3D wavelet transform. *Icarus* 207, 66–81.
- Campbell-Brown, M.D., 2008. High resolution radiant distribution and orbits of sporadic radar meteoroids. *Icarus* 196, 144–163.
- Ceplecha, Z., 1967. Classification of meteor orbits. *Smiths. Contrib. Astrophys.* 11, 35–60.
- Ceplecha, Z., 1988. Earth's influx of different populations of sporadic meteoroids from photographic and television data. *Bull. Astron. Inst. Czechosl.* 39, 221–236.
- Di Sisto, R.P., Fernández, J.A., Brunini, A., 2009. On the population, physical decay and orbital distribution of Jupiter family comets: Numerical simulations. *Icarus* 203, 140–154.
- Galligan, D.P., Baggaley, W.J., 2004. The orbital distribution of radar-detected meteoroids of the Solar System dust cloud. *Mon. Not. R. Astron. Soc.* 353, 422–446.
- Galligan, D.P., Baggaley, W.J., 2005. The radiant distribution of AMOR radar meteors. *Mon. Not. R. Astron. Soc.* 359, 551–560.
- Gartrell, G., Elford, W.G., 1975. Southern hemisphere meteor stream determinations. *Aust. J. Phys.* 28, 591–620.
- Grün, E. et al., 1985. Collisional balance of the meteoric complex. *Icarus* 62, 244–272.
- Gural, P.S., 2012. A new method of meteor trajectory determination applied to multiple unsynchronized video cameras. *Meteorit. Planet. Sci.* 47, 1405–1418.
- Holman, D., Jenniskens, P., 2013. Discovery of the Upsilon Andromedids (UAN, IAU #507). *J. Int. Meteor. Org.* 41, 43–47.
- Ipatov, S.I. et al., 2008. Dynamical zodiacal cloud models constrained by high resolution spectroscopy of the zodiacal light. *Icarus* 194, 769–788.
- Jacchia, L.G., Verniani, F., Briggs, R.E., 1967. Analysis of the atmospheric trajectories of 413 precise photographic meteors. *Smith. Contrib. Astrophys.* 10, 1–139.
- Jenniskens, P., 2006. *Meteor Showers and Their Parent Comets*. Cambridge University Press, Cambridge, UK, 790pp.
- Jenniskens, P., 2008a. Meteoroid streams that trace to candidate dormant comets. *Icarus* 194, 13–22.
- Jenniskens, P., 2008b. Mostly dormant comets and their disintegration into meteoroid streams: A review. *Earth Moon Planets* 102, 505–520.
- Jenniskens, P., 2012. Mapping meteoroid orbits. *Sky Telescope* 87, 20–25.
- Jenniskens, P., Gural, P.S., 2011. Discovery of the February  $\eta$ -Draconids (FED, IAU#427): The dust trail of a potentially hazardous long-period comet. *J. Int. Meteor. Org.* 39, 93–97.
- Jenniskens, P., Nėnon, Q., 2016. CAMS verification of single-linked high-threshold D-criterion detected meteor showers. *Icarus* 266, 371–383.
- Jenniskens, P. et al., 2009. On how to report new meteor showers. *J. Int. Meteor. Org.* 37, 19–20.
- Jenniskens, P. et al., 2011. CAMS: Cameras for Allsky Meteor Surveillance to establish minor meteor showers. *Icarus* 216, 40–61.
- Jenniskens, P., Gural, P.S., Holman, D., 2012. The established meteor showers as seen in video meteoroid orbit surveys. In: Gyssens, M., Roggemans, P. (Eds.), *Proceedings of the International Meteor Conference, La Palma, 20–23 September 2012*. The International Meteor Organization, Belgium, pp. 38–43.
- Jenniskens, P. et al., 2016a. The established meteor showers as observed by CAMS. *Icarus* 266, 331–354.
- Jenniskens, P. et al., 2016b. CAMS confirmation of previously reported meteor showers. *Icarus* 266, 355–370.
- Jopek, T.J., 1993. Remarks on the meteor orbital similarity D-criterion. *Icarus* 106, 603–607.
- Jopek, T.J., Kanuchová, Z., 2014. Current status of the IAU MDC meteor shower database. In: Jopek, T.J. et al. (Eds.), *Meteoroids 2013*. Proc. of the Astron. Conf. Held at A.M. University, Poznan, Poland, August 26–30, 2013. A.M. University Press, pp. 353–364.
- Kanamori, T., 2009. A meteor shower catalog based on video observations in 2007–2008. *J. Int. Meteor. Org.* 37, 55–62.
- Koukal, J. et al., 2014. Some interesting meteor showers in EDMOND database. *J. Int. Meteor. Org.* 42, 7–13.
- Neslusan, L., Svoren, J., Porubcan, V., 1998. A computer program for calculation of a theoretical meteor-stream radiant. *Astron. Astrophys.* 331, 411–413.
- Nesvorný, D. et al., 2010. Cometary origin of the zodiacal cloud and carbonaceous micrometeorites. Implications for hot debris disks. *Astrophys. J.* 713, 816–836.
- Nesvorný, D. et al., 2011. Dynamical model for the zodiacal cloud and sporadic meteors. *Astrophys. J.* 743, 129–145.
- Nilsson, C.S., 1964. A southern hemisphere radio survey of meteor streams. *Aust. J. Phys.* 17, 205–256.
- Öpik, E.J., 1958. *Physics of Meteor Flight in the Atmosphere*. Interscience Publishers, New York, 174pp.
- Poynting, J.H., 1903. Radiation in the Solar System: Its effect on temperature and its pressure on small bodies. *Philos. Trans. R. Soc. Lond. A* 202, 525–552.
- Robertson, H.P., 1937. Dynamical effects of radiation in the Solar System. *Mon. Not. R. Astron. Soc.* 97, 423–437.
- Rudawska, R., Jenniskens, P., 2014. New meteor showers identified in the CAMS and SonotaCo meteoroid orbit surveys. In: Jopek, T.J. et al. (Eds.), *Meteoroids 2013*. Proc. Astron. Conf. Held at A.M. University, Poznan, Poland, August 26–30, 2013. A.M. University Press, pp. 217–224.
- Segon, D. et al., 2014. Results of CMN 2013 search for new showers across CMN and SonotaCo databases III. *J. Int. Meteor. Org.* 42, 227–233.
- Steakley, K., Jenniskens, P., 2013. Discovery of the February  $\epsilon$  Virginids (FEV, IAU#506). *J. Int. Meteor. Org.* 41, 109–111.
- Taylor, A.D., Elford, W.G., 1998. Meteoroid orbital element distributions at 1 AU deduced from the Harvard Radio Meteor Project observations. *Earth Planets Space* 50, 569–575.
- Veres, P., Tóth, J., 2010. Analysis of the SonotaCo video meteor orbits. *J. Int. Meteor. Org.* 38, 54–57.
- Weryk, R.J. et al., 2013. The Canadian Automated Meteor Observatory (CAMO): System overview. *Icarus* 225, 614–622.
- Whipple, F.L., 1954. Photographic meteor orbits and their distribution in space. *Astron. J.* 59, 201–217.
- Wiegert, P.A. et al., 2013. The return of the Andromedids meteor shower. *Astron. J.* 145, 70–81.
- Williams, I.P., 2011. The origin and evolution of meteor showers and meteoroid streams. *Astron. Geophys.* 52, 2.20–2.26.
- Wyatt, S.P., Whipple, F.L., 1950. The Poynting–Robertson effect on meteor orbits. *Astrophys. J.* 111, 134–141.